Development of an Overpressure Test Cell and Sensitivity Study for Double Beta Experiments

Magdalena Eisenhuth

Mai 13, 2024
Version: Final Version

JOHANNES GUTENBERG
UNIVERSITÄT MAINZ

Fachbereich 08
Institute of Physics
ETAP AG Wurm

Master thesis

Development of an Overpressure Test Cell and Sensitivity Study for Double Beta Experiments

Magdalena Eisenhuth

1. Reviewer Prof. Dr. Michael Wurm
Institute of Physics
Johannes Gutenberg-Universität

2. Reviewer Prof. Dr. Sebastian Böser
Institute of Physics
Johannes Gutenberg-Universität

Supervisors Prof. Dr. Michael Wurm and Manuel Böhles

Mai 13, 2024

Magdalena Eisenhuth
Development of an Overpressure Test Cell and Sensitivity Study for Double Beta Experiments
Master thesis, Mai 13, 2024
Reviewers: Prof. Dr. Michael Wurm and Prof. Dr. Sebastian Böser
Supervisors: Prof. Dr. Michael Wurm and Manuel Böhles

Johannes Gutenberg-Universität
ETAP AG Wurm
Institute of Physics
Fachbereich 08
Staudingerweg 7
55128 Mainz

Abstract

The investigation of double beta decay and neutrinoless double beta decay is crucial for understanding the nature of neutrinos. In this context, the krypton ^{78}Kr stands out as a promising candidate. Understanding the behaviour of krypton dissolution in liquid scintillator is crucial for a potential new experiment named NuDoubt^{++}. This thesis explores the progress in developing an overpressure scintillator test cell to examine the loading factor and transparency and scintillation properties. The test cell build of stainless steel can hold around $550\,\mathrm{mL}$ of liquid scintillator and features the possibility of loading krypton and other gases while being able to investigate their transparency properties. The focus of the second part of this thesis is the investigation of the sensitivity of potential detectors with the goal of measuring the double and neutrinoless double beta plus decay. This is done for a proposed experiment called NuDoubt^{++} and for the already existing OSIRIS detector. Both study showed potential discovery with the need of a combination of pressure loading and enrichment techniques and further background mitigation strategies.

Zusammenfassung

Die Untersuchung des doppelten Betazerfalls und des neutrinolosen doppelten Betazerfalls ist entscheidend für das Verständnis der Natur der Neutrinos. In diesem Zusammenhang erweist sich das Krypton ^{78}Kr als vielversprechender Kandidat. Das Verständnis des Verhaltens der Kryptonauflösung in flüssigem Szintillator ist entscheidend für ein mögliches neues Experiment namens NuDoubt^{++}. In dieser Arbeit werden die Fortschritte bei der Entwicklung einer Überdruck-Szintillator-Testzelle zur Untersuchung des Beladungsfaktors und der Transparenzeigenschaften untersucht. Die aus rostfreiem Stahl gefertigte Testzelle kann rund$550\,\mathrm{mL}$ Flüssigszintillator fassen und bietet die Möglichkeit, Krypton und andere Gase zu laden und gleichzeitig deren Transparenzeigenschaften zu untersuchen. Der Schwerpunkt des zweiten Teils dieser Arbeit liegt auf der Untersuchung der Empfindlichkeit potenzieller Detektoren mit dem Ziel der Messung des doppelten und neutrinolosen doppelten Beta-Plus-Zerfalls. Dies geschieht für ein vorgeschlagenes Experiment na-

mens NuDoubt^{++} und für den bereits existierenden OSIRIS-Detektor Beide Studien zeigten ein Entdeckungspotenzial, das eine Kombination von Druckbeladungs- und Anreicherungstechniken sowie weitere Strategien zur Verringerung des Hintergrunds erfordert.

Acknowledgement

First of all, I would like to thank my supervisor professor Michael Wurm for giving me the opportunity to explore this highly interesting field of physics and for having faith in my abilities.
And I would like to thank professor Sebastian Böser for his willingness to be the second reviewer.
I must thank Arshak and Daniela for they patience and kindness they showed towards me while sharing their knowledge.
Thank you the whole working group especially the office for welcoming me and always having an open ear for me. I also want to thank the office next door for the accepting the invasion.

My special thanks goes to my family for the love and support they give me. I feel immensely lucky to have grown up in your warmth and joy leading to independence.

Contents

1 Introduction

"The year is 2024. The Standard Model of physics is entirely known. Well not entirely ... One small group of fermions still holds out against the order. And life is not easy for scientist who try to figure out their mystery"

From the first postulation of neutrinos in the 1930s, the research around neutrinos has been an ongoing exploration. The small interaction probability rising the need for ever bigger detectors. With more research, discoveries like neutrino oscillations by the Super-K[1] and SNO[2] collaborations were made. This discovery proves that neutrinos have mass, which does not fit the Standard Model and new physics beyond the Standard Model is needed. An ongoing question in neutrino physics is the search to explore the nature of the neutrinos. The Dirac or Majorana nature of the neutrino could be explored by observing neutrinoless double beta decay ($0\nu2\beta$) [3]. Experiments with the aim of measuring this rare decay like KamLAND-Zen and GERDA reached an upper limit of the half life of the $0\nu2\beta$- of the order of $10^{26}\,\mathrm{years}$ [4][5]. The next generation of experiments requires larger concentration of 2β isotopes and higher energy resolution and most crucially is the elimination of background in the region of interest (ROI). The proposed NuDoubt^{++} (Neutrino Double beta plus plus) experiment [6], with its novel scintillator and detector design, has the potential to fulfil all three of these requirements. This is done by using background mitigation techniques, including the information of Cerenkov and scintillation light and event topology, possible by using opaque slow scintillators. The double beta candidate is dissolved in the scintillator as already successfully demonstrated in KamLAND-ZEN [7] but for a larger double beta isotope concentration an improved loading is necessary. This thesis investigates two aspects for future double beta experiments. The first is the development of a scintillator test cell that allowed the loading of gas under pressure, measuring the loading factor and the optical and scintillation properties of these loaded scintillators. The second aspect is the investigation of the sensitivity of the detector under different assumptions of concentration of double beta isotopes in the scintillator and background discrimination.

In chapter 2 a short introduction into the current knowledge of neutrino physics is given. Neutrinos in the standard model and beyond, introducing the concept of Majorana neutrinos and the physics behind the double beta decay, are discussed as

well as the physics of liquid scintillators and their loading with gas. Those concepts will be used in chapter 3 to motivate the need of pressure loading by taking a closer look at the current state of loading Krypton. Here the requirements of the test cell are explained in order to understand the design choices made in the process. In chapter 4 this design process of the cell is described. Starting with the introduction of the general shape and especially taking a closer look at the inside of the test cell and describing ways of improving the test cell for measurements of the loading factor. The construction of the test cell and the whole measuring infrastructure is discussed in chapter 5 together with the first transparency measurements comparing the test cell to a regular cuvette. The sensitivity study performed for the NuDoubt^{++} experiment is presented in chapter 6 together with the discussion of the background rates and their discrimination strategies. This was also done for OSIRIS, another liquid scintillator experiment. In the last chapter 7, the results and the progress made in the scope of this thesis are summarised.

Theoretical Background

2

> "Nothing in life is to be feared, it is only to be understood. Now is the time to understand more, so that we may fear less." Marie Curie, physicist, chemist and first woman winning a Nobel prize

The aim of this chapter is to provide the background needed for understanding the physics of this thesis. This is based on research results made in the last century till today and text books especially [8] for the neutrino heavy theory part.

2.1 Neutrinos in and Beyond the Standard Model

The existence of the neutrino was first postulated by Pauli 1930 [9] trying to explain the continuous spectrum of the β decay puzzling the scientific community back then. The quest for the first measurement of this new particle begun and was first detected at the Savannah River Plant, South Carolina by Clyde L. Cowan and Frederick Reines in 1956 [10], using the interaction of a proton and an anti electron neutrino created in the reactor nearby. Not long after with the help of neutrino beam produced of decaying pions ([11]), the second neutrino flavor, the muon neutrino was found. With the discovery of the third generation of fermions the existence of a third neutrino was postulated and first measured by the DONUT-Experiment 2000 [12]. These three flavours ν_e, ν_μ and ν_τ are now an integral part of the standard model of particle physics (SM) together with their corresponding anti neutrino. These fermions are electrically neutral, massless and with a spin of 1/2.

With the rise of ever bigger neutrino observatories appeared the discrepancies from the expected perfect SM world. In 1964 the Homestake experiment in South Dakota [13] measured only a third of the expected solar electron neutrino flux creating the famous "solar neutrino problem". The problem was "solved" with the measurement of the neutrino oscillation by the SNO [14] being not only sensitive to the electron neutrino like Homestake but also to the other two neutrino flavours resulting in the theory of neutrino oscillation and proof of a non-zero neutrino mass, physics beyond the SM.

However, no direct measurement of the neutrino mass could be made. The KATRIN experiment provides the currently best upper limit on the square of the effective neutrino mass $m_\nu = 0.85\,\mathrm{eV}$ [15]. The explanation of such small masses is still not clear. With the introduction of the Majorana formalism to the already established Dirac formalism, these small masses could be explained. The observation of the neutrinoless double beta decay will provide important understanding about the nature of the neutrino.

2.2 Double Beta and Neutrinoless Double Beta Decay

The double beta decay is a rare nuclear transition in which the atomic number (Z) increases by two units, while the number of nucleons (A) remains constant. This is the only decay channel for nuclei where the single β decay is forbidden by energy or spin configurations. In figure 2.1 the mass parabola can be seen showing the single β decay on the left and double beta configuration on the right. The y axis shows the semi-empirical mass formula $m(A, Z)$ featuring a pair binding energy term dependent on the nuclei configuration. For a normal beta decay to be possible the condition is $m(A, Z_0 - 1) > m(A, Z_0)$ as seen in the left case. This is not the case on the right side and the normal β is suppressed. The only way for these nuclei to decay is via double beta decay ($2\nu2\beta^-$ or $2\nu2\beta^+$).

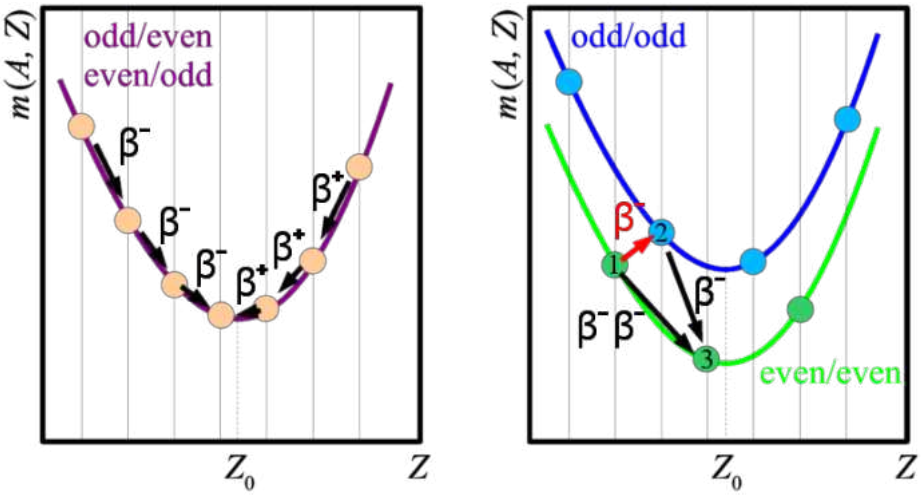

Fig. 2.1.: Mass parabola as a function of the ordering number Z. On the left a nuclei with odd/even mass number. On the right a nuclei with splitting of the mass parabola in even/even and odd/odd configurations. (Plot taken from [16])

In addition to the $2\nu2\beta^+$ decay two more decay modes including the possibility of electron capture (EC) are possible as can be seen in the following:

$$2\nu2\beta^+ : \quad (A,Z) \rightarrow (A,Z-2) + 2e^+ + 2\nu \tag{2.1}$$

$$2\nu\text{EC}\beta^+ : \quad (A,Z) + e^- \rightarrow (A,Z-2) + e^+ + 2\nu \tag{2.2}$$

$$2\nu2\text{EC} : \quad (A,Z) + 2e^- \rightarrow (A,Z-2) + 2\nu \tag{2.3}$$

Assuming that the mass of the electron/positron is orders of magnitudes smaller than the nucleus, the recoil energy is negligible and the entire energy $Q_{\beta\beta}$ is shared between the final state particles, creating a continuous spectrum as can be seen in figure 2.2. Here the energy of both electrons emitted in a $2\nu2\beta^-$ decay is shown. The

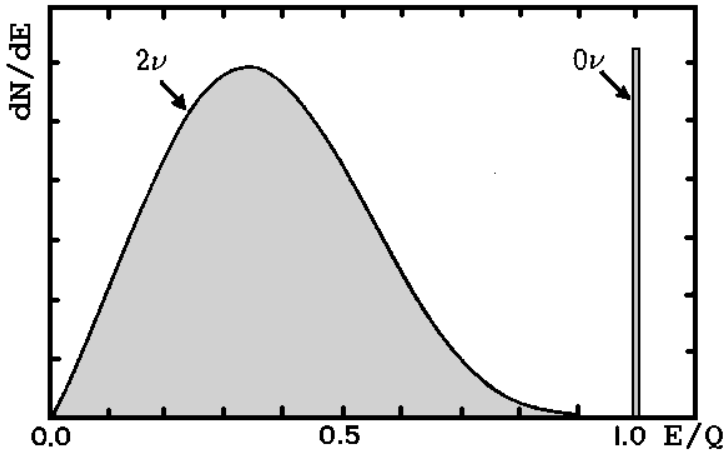

Fig. 2.2.: Decay spectrum of a $2\nu2\beta^-$ with the additional monoenergetic signal of the theoretical $\nu2\beta^-$ decay (plot taken from [17])

transition rate $\Gamma^{2\nu}$ or the reciprocal half life $\frac{1}{T^{2\nu_{1/2}}}$, of this process can be calculated using Fermi's golden rule:

$$\Gamma^{2\nu} = \frac{1}{T^{2\nu_{1/2}}} = G^{2\nu}(Q_{\beta\beta}, Z) \left| M^{2\nu} \right|^2 \tag{2.4}$$

with the phase space factor $G^{2\nu}$ describing the overlap of the phase space of all four leptons involved in the process. $M^{2\nu}$ is the nuclear matrix element taking the nuclear structure into account.

The postulation by E. Majorana [18] discusses symmetries between neutrinos and antineutrinos and implies the existences of the neutrinoless double beta decay ($0\nu2\beta$) similar to the $2\nu2\beta$ but only with the emission of two electrons/positrons. This creation of two leptons without leptonic anti particles violates the lepton number symmetries established in the SM. In the case where no neutrino is emitted, all the

energy has to be carried by the electron/positron creating the monoenergetic line in figure 2.2 at the end point of the 2ν spectrum. In figure 2.3 the Feynman diagram of the normal and neutrinoless case can be seen on the left side. The neutrinoless decay process, as seen on the right, is caused by the exchange of a virtual neutrino transitioning to an antineutrino before getting absorbed at the second vertex. The

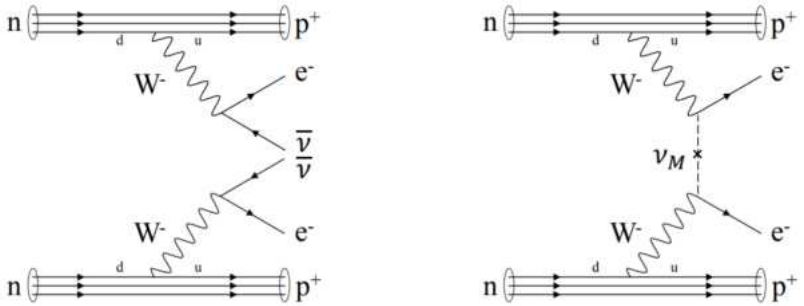

Fig. 2.3.: Feynman diagrams of the ordinary double beta decay (left) and the neutrinoless double beta decay (right) (Figure and caption taken from [19])

transition rate of this light exchange case can be described with:

$$\Gamma^{0\nu} = \frac{1}{T^{0\nu_{1/2}}} = G^{0\nu}(Q_{\beta\beta}, Z) \sum_x \left| M_x^{0\nu} \right|^2 |f_x(m_i, U_{ei})|^2 \tag{2.5}$$

introducing a factor $f_x(m_i, U_{ei})$ containing the effective Majorana mass term for neutrinos thus physics beyond the SM explained in detail in [20].

The observation of this decay has not been successful yet. Because of the low transition rate, detectors have to face new challenges described in the following. When choosing the double beta isotope a high Q-value, especial over the γ-line of ^{208}Tl with an energy of $2.615\,\mathrm{MeV}$ is favorable since this reduces the background in the region of interest (ROI). Good energy resolution and background discrimination is key in order to identify the signal peak over the background. On the other hand, increasing the double beta isotopes used in the experiment is beneficial, but most of the candidates have a natural fraction of less than $10\,\%$, increasing the need for enrichment thus increasing the cost of the experiment. For the detection of the neutrinoless beta decay new detector techniques have to be developed. Here the NuDoubt^{++} experiment tries to make the step in this regime.

2.3 The NuDoubt^{++} Experiment

The **Neu**trino **Dou**ble **b**e**t**a **plus plus** (NuDoubt^{++}) detector is a novel detector concept with the potential to be up to those problems [6]. By taking a similar path as the already successful of KamLAND-ZEN [4], loading the detector with double beta isotope the NuDoubt^{++} detector aims for higher loading factors, better energy resolution and improved particle identification powers. The discrimination power especially for electron and gamma signals is realised by using $2\beta^+$ isotopes creating a different signature in the detector than electrons or gammas. This information is taken from the difference of scintillation to Cerenkov light created by the particle. Also by using a novel type of scintillator called opaque scintillator and an array of OWLs as read out fibers the topology of the decays can be evaluated also providing information about the energy and particle type.

2.4 Principles of Scintillators

For many experiments including the NuDoubt^{++} detector scintillators are an essential part of the detector design. In the following the working principle is described, based on Knoll, Glenn F [21].

A scintillator is a material which is excited by incoming particles and emits photons in the process of deexcitation. Scintillators can be made out of a variety of materials and are grouped accordingly in organic and inorganic scintillators. Inorganic scintillators are mostly doped crystals whereas organic scintillators are characterized by the presence of aromatic hydrocarbon compounds. In the following the emission principle for scintillators will be displayed.

The excitation of the scintillator is due to interaction of the scintillation material with an electrically charged particle. Depending on the particles energy, this leads to an excitation of an electron into higher energy levels or ionization of the molecule. Only the excitation can be used for the scintillation process. When returning into the ground state, a photon with the same energy as the energy difference between ground state and the lowest vibrational mode of the excited state is emitted. This process is called luminescence and can be divided into two different categories according to the multiplicity of the excited state. Long processes with state lifetimes in the order of $1\,\mu\mathrm{s}$ are called phosphorescence, short processes with $\tau \leq 10\,\mathrm{ns}$ are called fluorescence. For an organic scintillator the short decay constant arises from a direct deexcitation from excited to ground state without a change in multiplicity. This

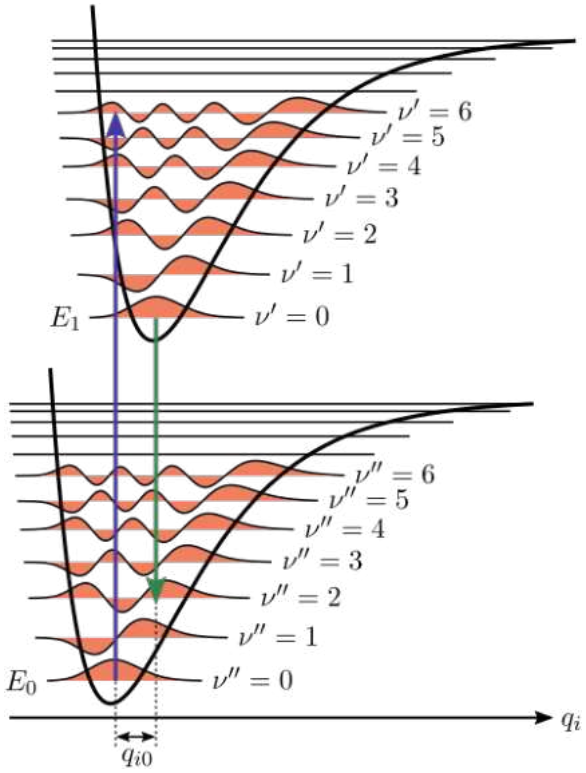

Fig. 2.4.: Schematic representation of the energy states scintillator molecules for a fixed internuclear distance q_{01}. ν'' are the vibrational states of the electronic ground state and ν' of the first excited electronic state (picture taken from [22])

happens usually if the electron is excited into a singlet state. For the phosphorescence a change in the electrons multiplicity is required, which needs a transition that is forbidden by quantum mechanics. A return to the ground state can also be achieved by interacting with another electron with the same multiplicity (usually between two triplet states), which is then called a delayed fluorescence. The emitted photon is in the same energy interval as the excitation energy of the electrons, therefore the reabsorption of this photon is very likely. This causes the material to be opaque for this wavelength and only few photons leave the material. Since only the emitted light can be detected, this is not ideal. Therefore a wavelength shifting material is added into the scintillator material. This leads to a decrease in the energy of the emitted photon and therefore increases the wavelength, preferably into the visible light spectrum. The principle behind this effect is the Franck-Condon-principle, which describes the favorable transition, where the emission time of the photon is relatively short in comparison to the nuclear motion. If the electron is excited as shown in figure 2.4 by the blue arrow, it will continuously emit energy until reaching the lowest excited state.

From there the preferable de-excitation is the transition shown in green. In this transition a photon is emitted with a lower energy than the one emitted by the scintillation material. Ideally the shift is made into a wavelength range where the scintillator material is as transparent as possible.

2.5 Dissolving Gas in Liquid

In the following the process of dissolving a gas in liquid and ways of enhancing this are discussed. When a gas phase is brought in contact with a liquid phase, a fraction of the gas particles will dissolve in the liquid creating an equilibrium of gas particles entering and leaving the liquid. When increasing the pressure as shown in figure 2.5 the new equilibrium features a higher concentration of gas in the liquid. The amount of gas that can be dissolved in a liquid is described by Henry's law creating a proportionality between the concentration of gas particles in the liquid and the partial pressure of the gas. The proportionality constant H, the so called Henry constant, can be described as follows:

$$H = \frac{p}{C} \tag{2.6}$$

with the concentration C and pressure p. The shape of the equation can differ

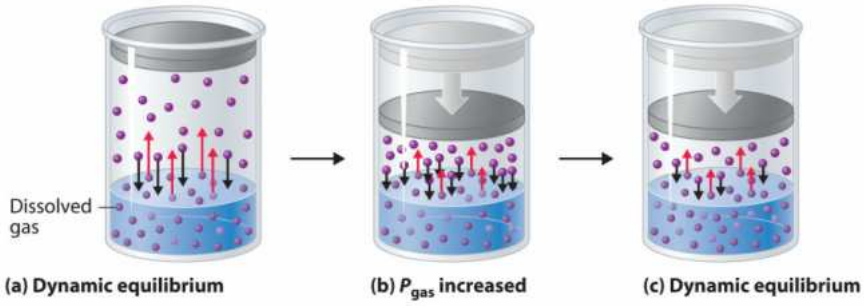

Fig. 2.5.: working principle of increased gas concentration in a liquid when incising the pressure. a) gas entering and leaving the liquid is in a dynamic equilibrium. b) with an increase in pressure increasing density in the gas phase, and c) a new equilibrium settles in. (picture taken from [23])

depending on the unit of the Henry constant and concentration type but always with the same physical outcome. By increasing the pressure a new equilibrium will form

and according to Henry's law the concentration of dissolved particles is higher. The Henry constant needs to be determined for each pair of gas and liquid.

3 Motivation of Krypton Loading

> "Everything was so new - the whole idea of going into space was new and daring. There were no textbooks, so we had to write them.", Katherine Johnson, mathematician

In this chapter the basic principles for the measurement and requirements of the test cell are explained. They are needed to motivate and understand the design choices in the next chapter and give an overview over the measuring techniques. First the initial idea for this thesis, the introduction of the loading factor and its possible increase are presented followed by the measuring techniques that are possible in the available lab. At the end of this chapter the requirements of the test cell are deduced.

3.1 Loading Factor of Krypton in Liquid Scintillator

The goal of this section is to give an idea about what orders of magnitude of krypton can be dissolved in liquid scintillators (LS) and how much this is improved by applying pressure.

As described in the theoretical background in section 2.5 the amount of gas that can be dissolved in a liquid depends on the pressure. In this thesis it is called Loading Factor. In our case we look at krypton in a liquid scintillator (LS) and apply Henry's law (equation 2.6). The following considerations give an idea of how much krypton can be expected to dissolve in LS. In order to find well fitting literature values of Henry's constant the assumption is made that toluene is chemically similar to the LS in use. For the pair of krypton (gas) in toluene (liquid) the Henry constant is $294\,\mathrm{atm}$ [24] which results in a mole fraction of 3.4×10^{-3} at $1\,\mathrm{atm}$ and $20\,^{\circ}\mathrm{C}$. That is comparable to the values calculated in [25] that show the temperature dependent solubility. Using this as a starting point, the pressure dependent concentration $C(p)$ can be calculated. This mole fraction can then be converted into the number of krypton atoms in a given amount of toluene using equation 3.1. Using the

molar mass $M_{toluene} = 92.14\,\mathrm{g/mol}$, one can find the number of krypton atoms in $m_{toluene} = 1\,\mathrm{kg}$ of toluene.

$$\frac{N_{kr}}{\mathrm{kg}_{toluene}} = \frac{C(p) \cdot \frac{m_{solvent}}{M_{solvent}}}{C(p) - 1} \cdot Na \tag{3.1}$$

The computed values for the different noble gases argon, krypton and xenon can be seen in figure 3.1with Henry constants taken from [24]. Argon is shown because krypton is not that cheap and the idea is to use argon to test the loading process of the test cell. Xenon is added for comparison with the already existing experiment KamLAND-Zen using xenon as double beta emitter [26][27]. This latter is used as a baseline giving an idea on what levels need to be reached with pressurising. On the left plot the number of atoms in $1\,\mathrm{kg}$ toluene are shown while the right plot shows the mass of those atoms. In order to keep a good comparability between different noble gases, the y axis is scaled in a logarithmic way. Otherwise, the relationship between the amount of gas dissolved in the LS increases linear with increasing pressure. By increasing the loading pressure to $6\,\mathrm{bar}$ one can see that even more krypton atoms can be dissolved in the scintillator compared to xenon at normal pressure. For this reason putting the system under pressure is a promising way of improving the statistics for future double beta experiments. Possible ways to measure and quantify this effect are described in the following section. For this a test cell was built which is described in more detail in chapter 4.

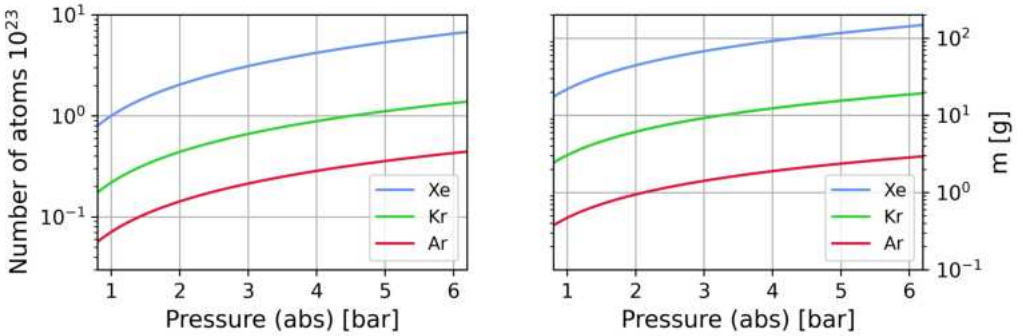

Fig. 3.1.: Comparison of the loading factor for different noble gases. The left plot shows the number of atoms that can be dissolved in $1\,\mathrm{kg}$ of toluene for different noble gases, the right plot the equivalent in mass.

3.2 Loading Factor Measuring Techniques

There are several ways of measuring the loading factor. They will be introduced in this section to give an idea what needs to be kept in mind for the design process of the test cell, what materials to use and what additional parts are needed.

The simplest method is to weigh the cell before and after loading it with Krypton. On the right side of figure 3.1 one can see, that when loading one $1\,\mathrm{kg}$ LS, only $19\,\mathrm{g}$ additional weight is added by the krypton. To be able to measure this effect a scale is needed able to measure several kg with a $100\,\mathrm{mg}$ accuracy. For this kind of measurement it is crucial for the amount of liquid in the test cell to stay constant. This must be taken into account when filling the system with krypton to ensure that no LS is lost.

The second option is to monitor the pressure of the system. By installing a manometer directly at the krypton bottle the amount that was used in the process can be calculated under the assumption of an ideal gas. By installing a manometer at the system of the test cell the pressure drop could be monitored. Filling of the test cell with a starting pressure and then closing the inflow of additional krypton gas, since the new equilibrium between krypton and LS is not established instantly, will lead to a pressure drop until the dynamic equilibrium is created. The loading factor can be calculated from this pressure drop by knowing the volume of LS and pf the piping. Because the volume of the piping should be kept as small as possible in order to not waist a large amount of krypton, the pressure drop is large and easy to spot. But this also means that the initial pressure must be correspondingly higher than the pressure at which the loading factor is measured. So the the full pressure range potential of the test cell cannot be used for loading.

The last technique that is discussed here is the use of the unstable krypton isotope ^{85}Kr. This method is often used when measuring the concentration of Krypton in the ocean [28] or the diffusion i.e. in plastic scintillators [29]. ^{85}Kr decays via beta minus decay emitting an electron up to $0.687\,\mathrm{MeV}$ with a half life of $10.756\,\mathrm{a}$ [30]. By using a scintillator as a solvent, the test cell can also act as a detector. It will emit light when this (or any) decay takes place in the test cell. By counting the frequency of these events one can put a number on how much ^{85}Kr is dissolved in the LS. With the knowledge of the isotopic signature the total amount of krypton atoms can be calculated. Without the exact isotopic signature only the relative increase of the loading can be measured. For this method it is also crucial to know the volume of the LS where the ^{85}Kr decays are observed.

Since all of these methods are independent of each other they can all be implemented. For the first method a suitable scale is needed and for the second the manometers need to feature a scale with suitable accuracy but especially the information about how much krypton is taken from the bottle can provide useful informations. The most promising method is the third option, the measurement of the decay of ^{85}Kr with the LS witch is part of the experiment in any case.

3.3 Requirements of the Scintillator Test Cell

As seen in the sections before in order to make the loading factor measurement, the test cell needs to include a list of functions and restrictions that will be explained in this section. This list acts as reference for the design choices made in the following chapter 4.

In general to be able to measure the loading factor at different pressures, the test cell needs to be built liquid and gas tight and pressure resistant. For the scope of this thesis a test cell holding up to $5\,\mathrm{bar}$ over pressure (relative to $1\,\mathrm{bar}$ absolute) is the goal. As seen in figure 3.1 and its discussion these $5\,\mathrm{bar}$ are already a reasonable baseline for a double beta plus experiment. Because of the use of LS, the test cell must be constructed of scintillator resistant material. On the one hand to prevent leakage and on the other hand and more imported to prevent unwanted reactions between the material and the LS leading to a decrease of the scintillator quality. These two requirements can be met by choosing the right materials.

Besides the measurement of the loading factor the optical and scintillation properties of the loaded scintillator are of interest The transparency measurement can be made in the already in place Prekin Elmer UV-Vis spectrometer Lam 850 [31]. The requirement of the cell to fit in this device introduces very tight size constraints, as seen in figure 3.2. The red box representing the usable space. The yellow lines show the path of light through the spectrometer. Path 1 is the reference path where, as seen in the picture, also a cuvette holder can be mounted. In the picture a $10\,\mathrm{cm}$ cuvette holder is placed, showing what space is left for the test cell. Path 2 is used for the text cell. For a useful transparency measurement the cell needs to include a pair of UV transparent windows in the height of the light path ($8\,\mathrm{cm}$). Those windows are also needed to be able to collect the light emitted from the ^{85}Kr beta decay. This light collection is performed using two PMTs which need to be attached to the cell at the windows described before. To load the test cell with krypton a suitable loading

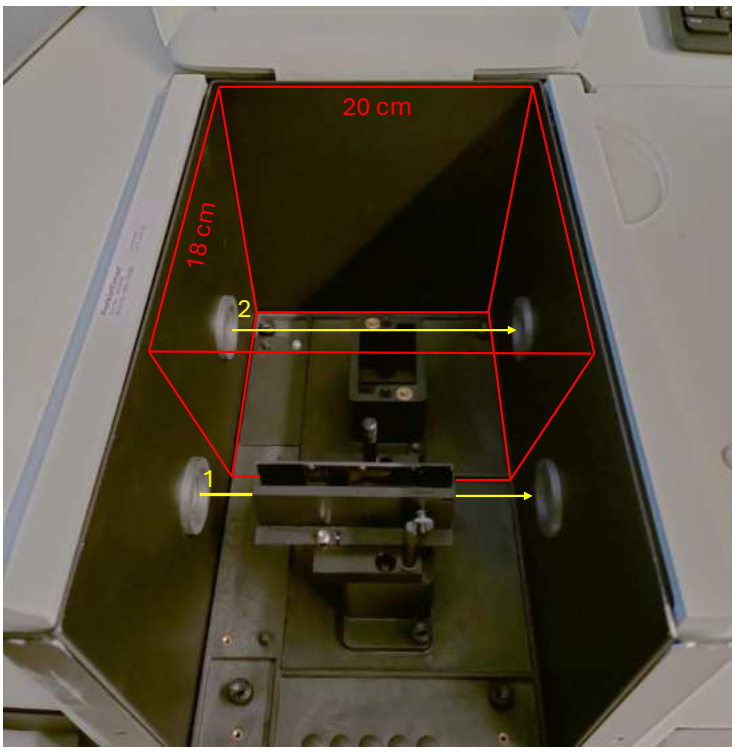

Fig. 3.2.: View inside the UV-Vis spectrometer Perkin Elmer Lam 850 [31] where the cell needs to fit in. The red box shows the space available for the test cell, the yellow arrows represent the two usable light paths.

system is necessary. This system needs to fit in the spectrometer or be detachable while still maintaining the pressure.

With those requirements in mind, the following sections show in detail the design of the test cell and the adaptations made for improvement along the progress of the work. It is also shown what has to be observed when loading the cell with liquid scintillator and gas and how the measurement setup has to be designed if needed. All these considerations can serve for the design of a large scale NuDoubt++ detector.

4 Design and Simulation of a Scintillator Test Cell

> "All sorts of things can happen when you're open to new ideas and playing around with things.", Stephanie Kwolek, chemist

The aim of this chapter is to explain the design process of a test cell for measuring and quantifying the loading factor of krypton in liquid scintillators and to explain the filling system. With the requirements from the previous chapter in mind, the main body of the test cell has been designed and is explained in the first sections, followed by a simulation using this initial design and looking for improvements in light collection and energy resolution. The focus then shifts to the filling system, explaining the idea behind it and the various parts required.

4.1 Geometry of the Test Cell

As the main constraint on the size of the test cell is the need to fit inside the spectrometer, this is the starting point of the design process. In order to maximise the volume of the cell, the filling system can be removed from the cell without depressurisation leaving more room for the test cell.

In figure 4.1 the digital sketch of the main body of the cell is shown. For visualisation purposes the cell is cut open in order to see how the parts fit together. For the full details on the dimensions of the cell design, the technical drawings can be found in section A.1. The main body of the test cell consists of 5 different stainless steel parts. The red part in the middle is made of a $107\,\mathrm{mm}$ long tube with an inside diameter of $50\,\mathrm{mm}$ and a wall thickness of $4\,\mathrm{mm}$. A flange has been welded to this pipe which is designed for pressures up to $5\,\mathrm{bar}$. The blue and green flanges are designed in a way to hold the UV transparent window in between, leaving an opening with a diameter of $54\,\mathrm{mm}$ on each side. The window itself is made of $8\,\mathrm{mm}$ thick UV transparent acrylic glass (PLEXIGLAS ®GS, UV-durchlässig Farblos 2458, Farblos 2458 SC). The length of the optical part in the LS is with $129\,\mathrm{mm}$ longer than the cuvettes, this needs to be taken into account when analysing the results from the

transparency measurements. The two connecting pipes for filling the cell with LS and then loading it with Krypton are both located on one side. This is done to avoid loosing the same amount of space on the other side of the cell as well. Instead one of the two pipes extends inside the cell. The reason for that design is explained when talking about the loading process later in section 4.4.

To allow enough room for connectors at the end of the pipes on the outside, the blue flange piece has two $16\,\mathrm{mm}$ wide holes. The flanges are screwed to the main body using 12 M6 screws on each side, more than enough to withstand the $5\,\mathrm{bar}$ over pressure. For a tight seal two o-rings made of FPM (Viton ®) are used on each side. A smaller $60\mathrm{x}2\,\mathrm{mm}$ o-ring creating a seal between the window and the middle flange part and a big $120\mathrm{x}3\,\mathrm{mm}$ o-ring creating a seal between the main body flange and the middle flange. On each side, the blue most outer flange has four M4 thread

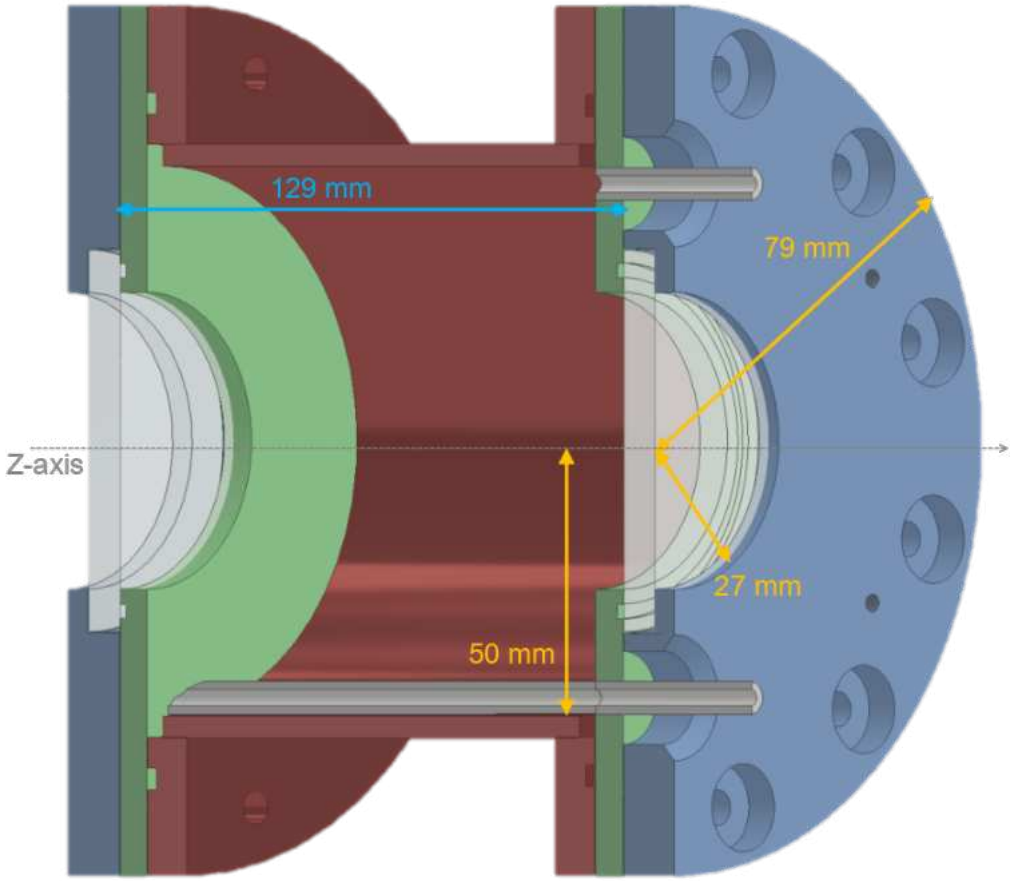

Fig. 4.1.: Half view of the digital sketch and dimensions of the test cell with each component having a different colour. In red is shown the middle part of the cell with a flange welded on at each side. The green and blue flanges hold the UV-transparent acrylic glass in place.

holes for different kinds of attachments. In this case they are used to hold the PMTs in place when measuring the ^{85}Kr decay. For this type of measurement it is useful to be able to get as much light out as possible to ensure enough statistics. How to increase the light collection of this test cell is the topic of the next section, where the focus lies on the inside of the cell.

4.2 Inner Surface of the Test Cell

In this section the light collection properties of the test cell will be explained and ways to improve it. The scintillation and Cerenkov light emitted from the electron of the ^{85}Kr beta decay in the volume of the LS needs to travel to the PMTs located at the windows of the test cell. The choice of the inner surface and its reflectivity properties are crucial to ensure that the light created in the decay is not absorbed by the test cell but guided to the PMTs. For the test cell, this can be achieved by focusing on the surface finish inside the cell. The different surface finish options in question are explained and evaluated further in this section.

The first option is to work with the material of the cell and try to make it as reflective as possible by electropolishing it, resulting in a mirror like specular reflective surface. The second option is to add some sort of coating to the inner walls. A coating like a barium sulfide based paint (BaSO4 coating) will produce a diffuse but highly reflective surface. Both principles of reflections can be seen in figure 4.2 showing specular reflection following the law of reflection $i = r$ at the bottom and diffuse reflection at the top where the incoming light (green) is reflected into light under different angles (yellow).

To decide which kind of combination of reflectivity and type of reflection is better suited for the test cell the two are compared in a simulation. This simulation is done on an already implemented GEANT4 simulation of a similar project. To make it work for the test cell a few changes had to be made.

First, the test cell geometry had to be implemented, which can be seen in figure 4.2. The red part represents the LS volume enclosed by the test cell in grey and a window on each side. The yellow circles are the logical detection volume and represent the photo cathode of the PMTs. The used geometry is a simplified model of the cell meaning only the important inner parts of the cell are accurate but wall thickness can vary from the original design without distorting the results. Another simplification made was replacing the whole cell material with the material properties of the chosen surface finish material.

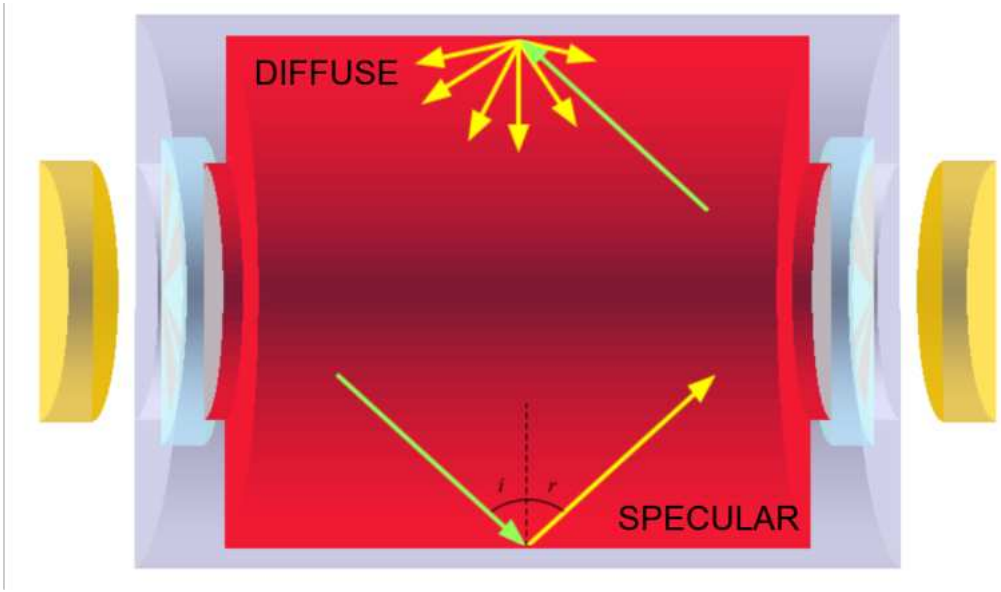

Fig. 4.2.: Picture of the geometry used in the GEANT4 simulation. In red the LS is shown encased by the test cell in grey. The photo cathode of the PMTs in yellow and two windows. In addition to the geometry the two different types of reflection are shown. At the top the diffuse reflection is shown, at the bottom specular reflection

The second adjustment to the simulation was the implementation of the material properties, especially the reflectivity for polished steel and the BaSO4 coating. For the polished steel the reflectivity was taken from Rubel et al.[32], while for the BaSO4 coating the values of different manufacturers were compared and the reflectivity was then set to 95% in the visible range. In comparison the highest reflectivity the polished steel can reach is about 60% for the wavelength region of UV to visible light.

The LS in this simulation is a mixture of linear alkyl benzene (LAB) as scintillator and solvent for $3\,\mathrm{g\,L^{-1}}$ polyphenylene oxide (PPO) and $15\,\mathrm{mg\,L^{-1}}$ bis-MSB as wavelengthshifter. The exact mixture of LS is not of importance in this simulation, but the relative changes when using different surface finishes. Therefore the mixture of LS was not adjusted for high light yield or decay times.

To compare the two mentioned surface finishes, polished steel and diffuse coating, the same simulation was performed with the different settings. The first simulation consisted of one electron in the middle of the cell and looking at the timing profile of this event for both materials. Using an electron particle gun one electron was created in the middle of the cell with an energy of $0.6\,\mathrm{MeV}$. In cylindrical coordinates this would be $r = 0\,\mathrm{mm}$, and $z = 0\,\mathrm{mm}$. In figure 4.3a one can see how this event (same energy and emission direction) looks like for the two PMTs in the first $20\,\mathrm{ns}$ after the first hit. It shows the sum of photons detected by both PMTs as a function

of time. The coating (blue surface) collects more photons than the steel surface (red). Since it is possible that the chosen direction is a coincidence, the simulation was additionally performed using the same energy and emission point but with an isotropic emission. In figure 4.3b this was averaged for 1000 runs. The time profile of the collected photons is shown for both instances.

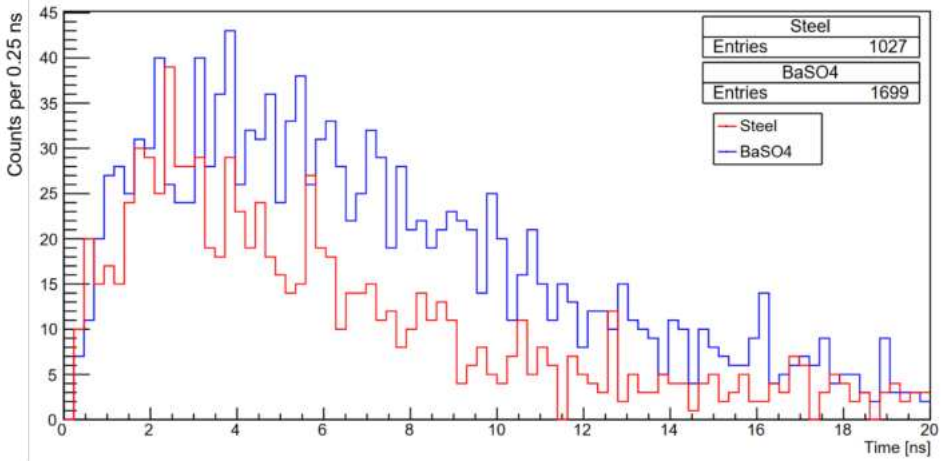

(a) 1 electron emitted in the middle of the cell in the same direction

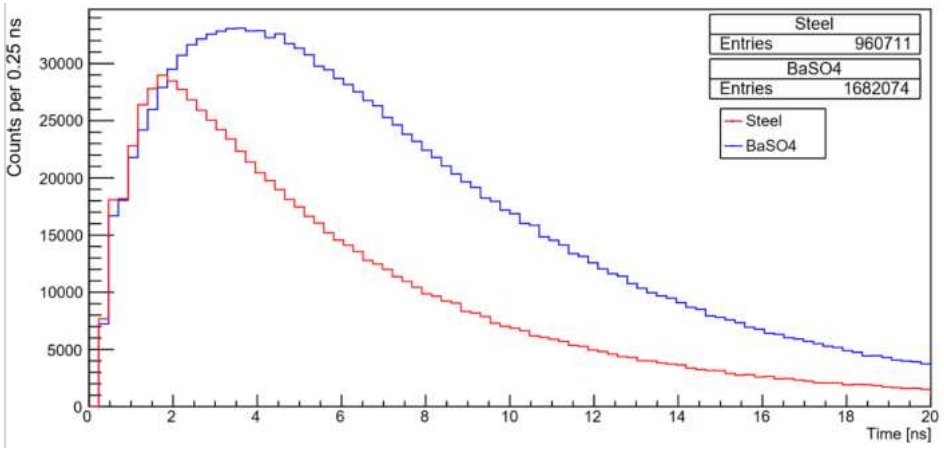

(b) 1000 electrons emitted isotropically in the center of the cell

Fig. 4.3.: Comparison of the time and intensity behaviour for the simulation of a) one and b) 1000 electrons in the middle of the test cell for two different surface finishes of the test cell. In blue the barium sulfide based coating and in red polished steel. The binning in both plots is the same $0.25\,\mathrm{ns}$

In this plot one can see that for early hits (up to $2\,\mathrm{ns}$) the polished steel surface (red) collects more photons in comparison to the BaSO4 coating (blue). After about $2\,\mathrm{ns}$ the BaSO4 coating takes over. Those are the photons that are either emitted in direct direction of the PMTs so without reflection or only reflected a few times without backscattering. In order for a photon to leave the test cell, many interactions must take place with the inner walls. It can be seen that the BaSO4 coating overtakes the

steel surface at the highest point of the steel curve. The BaSO4 coated cell peaks at around $3.5\,\mathrm{ns}$. The overall image shows that by using a BaSO4 coating the same amount of light can be collected for early hits and even more photons when looking at a larger time window and is therefore the material of choice.

While working on the simulation unfortunately the BaSO4 based coating which was in use for similar purposes in SHiP [33] caused problems and to avoid those the plan was changed to using PTFE (Teflon) instead. PTFE has similar reflectivity properties as the discussed coating and is therefore a suitable candidate. Inserting an additional hollow cylinder made of PTFE has a similar effect as coating the cell and comes with advantages that will be seen in section 4.3.

The next step in terms of simulation is to look at light collection from different points in the test cell by changing the emission point of the electron from the center along the r and z axis. This is done for 10 different positions in the cell and is summarized in figure 4.4. They have the same time profile as before but for emission points along the z axis with a fixed radius. In figure 4.4a the emission point of the simulated electron is varied along the z axis, so $r = 0\,\mathrm{mm}$ in $10\,\mathrm{mm}$ steps starting at $z = 0\,\mathrm{mm}$ represented by the purple curve and increasing until $z = 40\,\mathrm{mm}$ which is the red curve. In figure 4.4b the simulation results for a constant radius $r = 40\,\mathrm{mm}$ and again varying the emission point along the z axis. To reduce simulation time, the number of electrons simulated at each position is reduced to 500, resulting in a decrease of total PMT hits compared to the amount in figure 4.3b.

In the first plot, figure 4.4a, one can see that the overall number of collected photons increases the closer the emission point gets to the window. Comparing the center light collected from an event in the middle of the cell to the one closest to the window, the collected light increases by more than $35\,\%$. The second plot, figure 4.4b shows a different behaviour. The amount of collected photons varies much less and instead of increasing the light collection, it decreases slowly towards the window. This behaviour doesn't allow to distinguish between a high energetic event in the middle of the cell or a low energetic event near the window, resulting in a bad energy resolution. The measurement of the loading factor would benefit from a way to improve the energy resolution.

As mentioned before, the surface finish will be realised by using PTFE insets. Those come in handy now because the shape can be altered to a variation of different geometries. In order to test different shapes, further simulations were carried out, which are explained in the next section 4.3.

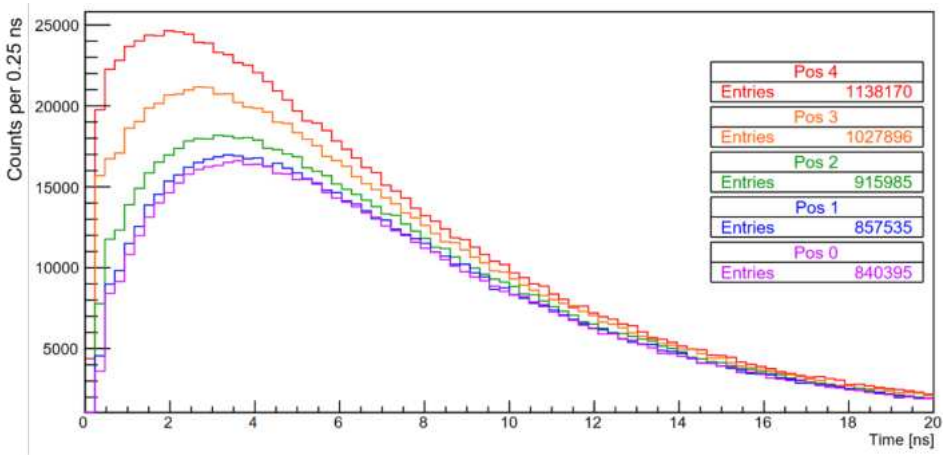

(a) $r = 0\,\mathrm{mm}$

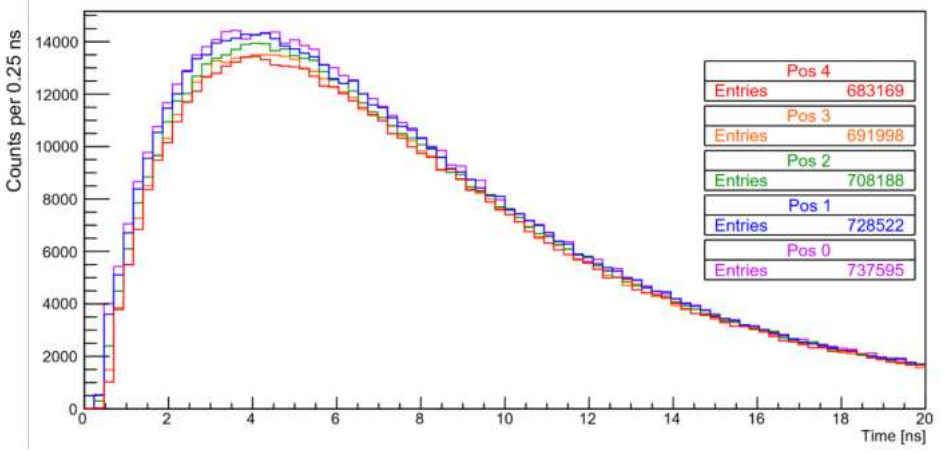

(b) $r = 40\,\mathrm{mm}$

Fig. 4.4.: Emission points of 500 e- with an energy of $0.6\,\mathrm{MeV}$ along the z axis at constant a) $r = 0\,\mathrm{mm}$ and b) $r = 40\,\mathrm{mm}$ for $z = 0\,\mathrm{mm}$(Pos 0) to $z = 40\,\mathrm{mm}$ (Pos 4) in $10\,\mathrm{mm}$. Different colours represent the position as described in the legend.

4.3 Additional Geometry to Increase Energy Resolution

This section looks in more detail at the behaviour of energy resolution seen in the previous section and at ways of improving it. This is done by discussing different geometric shapes that can be realized with PTFE and inserted into the test cell featuring four different geometry. In addition the empty cell with a cylindrical inset is added providing reference for the improvements. All shapes reduce the volume of the test cell, therefore a compromise between energy resolution and test cell volume and light collection is needed.

The different geometries that are considered in this section can be seen in figure 4.5. The first called sphere (top left) one is the induction of some sort of integrating

sphere with cylindrical extensions as big as the window. The second, called sphere ends, uses a similar idea but puts a half sphere at each end of the big cylinder in a way such that cutting the sphere at the end faces of the cell will yield a diameter matching the diameter of the window. The last two candidates called cones and parabolic look quite similar and have the same idea behind it, being to cut of the corner where the light collection is not good anyway. Starting small and getting bigger towards the middle. With an linear increase we get a cone shape and a parabolic shape with a parabolic increase.

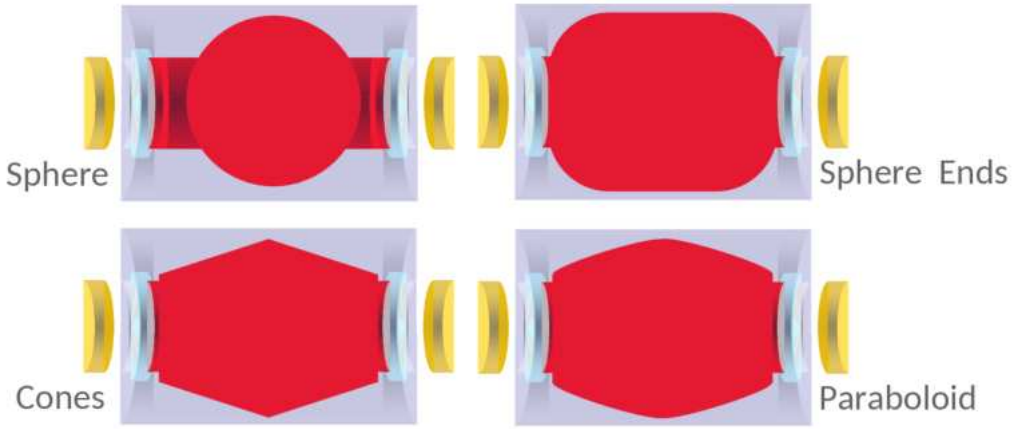

Fig. 4.5.: Geometry of the shapes used for simulating the energy resolution.

For the comparison of the different shapes and their performance regarding their energy resolution, a simulation was conducted, similar to the once before. In the following plots not the time profile is shown but only the total number of photons emitted from one event of both PMTs. The result of this can be seen in figure 4.6a. To save computation time, only the upper right quarter of the half cut plane was used. Every $1\,\mathrm{mm}$ in z and r direction ten photons where emitted isotropically. The plot shows the average amount of light collected from these 10 electrons with an energy of $0.6\,\mathrm{MeV}$ represented by colour. As comparison, there is also the plot of the cell with a cylindrical inset with a wall thickness of $0.2\,\mathrm{mm}$ which is refereed as empty cell. One can see, that any introduced geometry increases the light collection. The highest increase in collected light can be found in the cylindrical part of the sphere geometry near the window, raising the question how a purely cylindrical geometry with smaller radii would perform.

Therefore the same simulation was performed using cylindrical geometries with radii varying from $24\,\mathrm{mm}$ to $50\,\mathrm{mm}$ increasing by $2\,\mathrm{mm}$. A selection of those results can be seen in figure 4.6b. For a radius smaller than the opening radius of the window $30\,\mathrm{mm}$, the cylinders show the expected gradient of collected light increasing towards

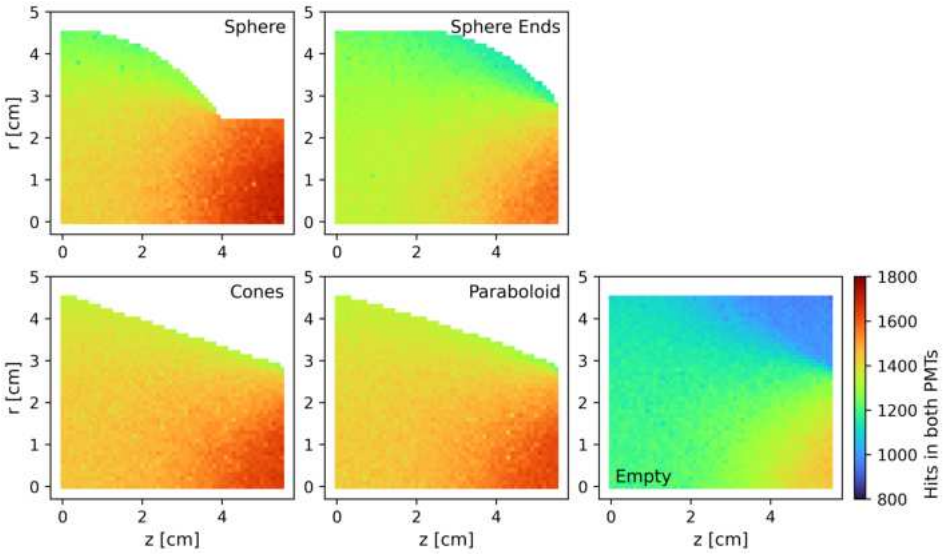

(a) Comparison of different shaped insets in the test cell, including the empty case which represents a cylindrical shaped inset with a wall thickness of 2 mm.

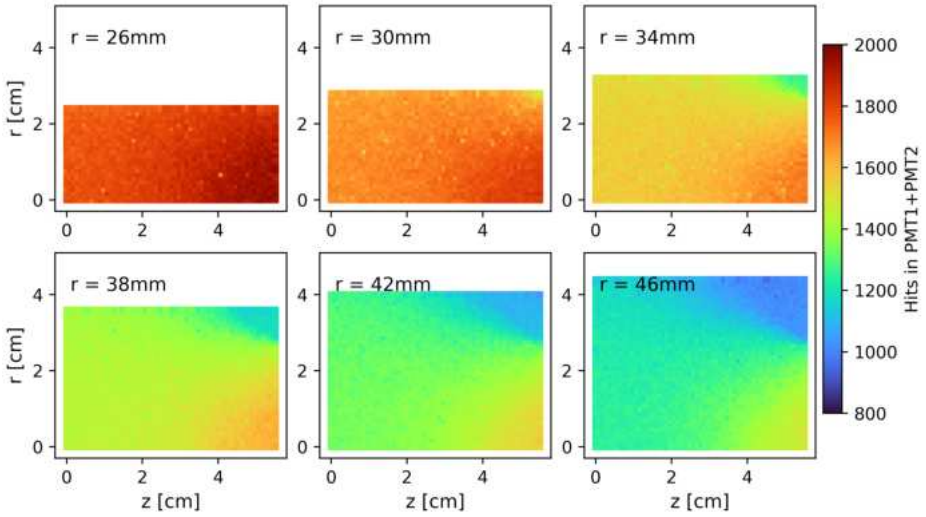

(b) Comparison of cylindrical shaped insets with varying radii.

Fig. 4.6.: Heat maps showing the amount of photons collected from the average of 10 electron event created at different positions in the volume with a spacing of . The colours represents the average amount of photons collected in both PMTs from 10 events at each point. Note that the colour map is not exactly the same for in both plots.

the window. For cylinders with larger radii, the inverted pattern can be seen when the radius is greater than the window. Only looking at the gradient a cylinder with the same radius as the opening of the window would be the best geometry but this would drastically reduce the volume of the test cell or a complete redesign in order to maximise the window size and use bigger PMTs. In the discussion of figure 4.6 only the plane of the cell is shown representing the whole volume. As the test cell is

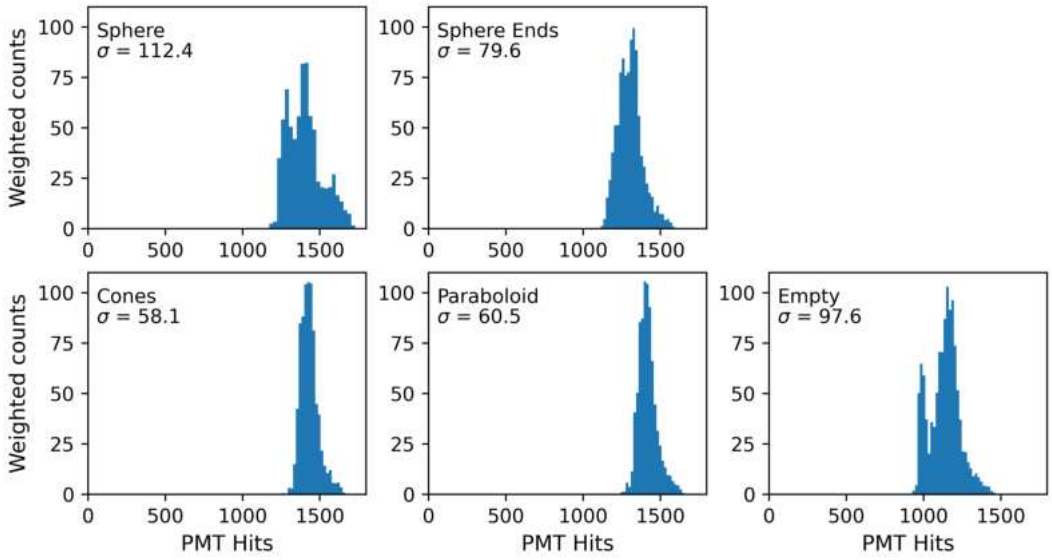

(a) Different geometries

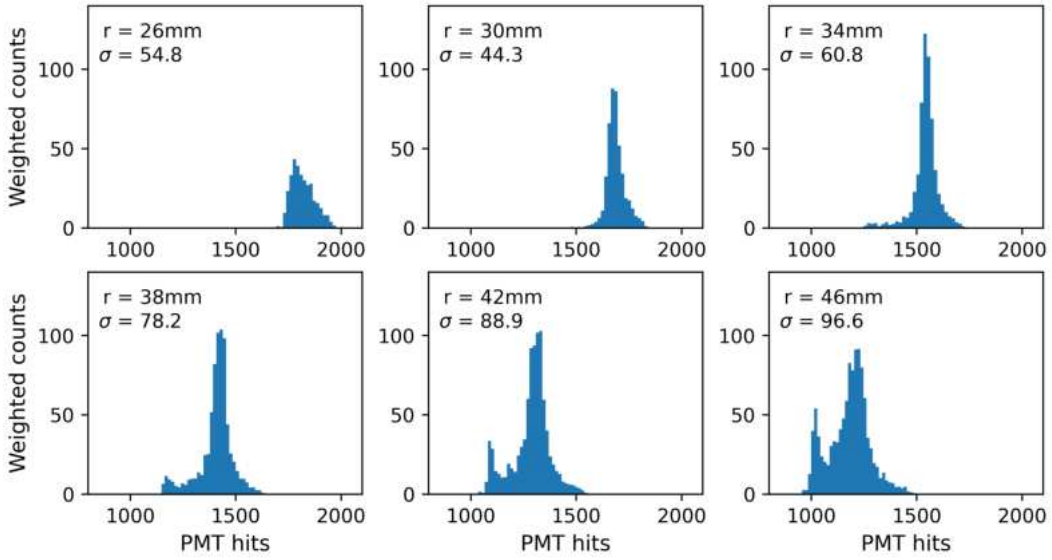

(b) Cylinders with different radii

Fig. 4.7.: Weighted histogram of the results shown in figure 4.6 with the standard deviation σ of each case.

cylindrical, events at large r are more frequent than those in the center. A geometry with good energy resolution in the centre and a seemingly small part deviating from it at large radii is not necessarily the best choice. To account for this effect, each event is weighted according to its radius. For the heat maps of the different shapes discussed above, the histograms generated in figure 4.7 show the frequency of how often a certain amount of light was collected in both PMTs. The upper figure 4.7a show the behaviour of the different geometries of figure 4.5 and figure 4.6a. In figure 4.7b, the same is shown for the cylindrical insets as previously discussed.

The histograms for both the sphere and the cylinder with $r > 38\,\mathrm{mm}$ show that there is a geometric factor in addition to the expected Gaussian distribution. The plots also show the standard deviation, which gives a first indication of the choice of geometry. The volume of the test cell is not taken into account. This is done by dividing by the square root of the number of events generated in the volume, favouring a geometry with a larger volume. These values can be found in figure 4.8. The result of varying the radius of the cylinders is shown, including radii not shown in the previous plots. In addition, the plot also shows the results of the different shapes at larger radii on the x-axis. Looking at the cylinders, there is a clear minimum at $30\,\mathrm{mm}$. This is also

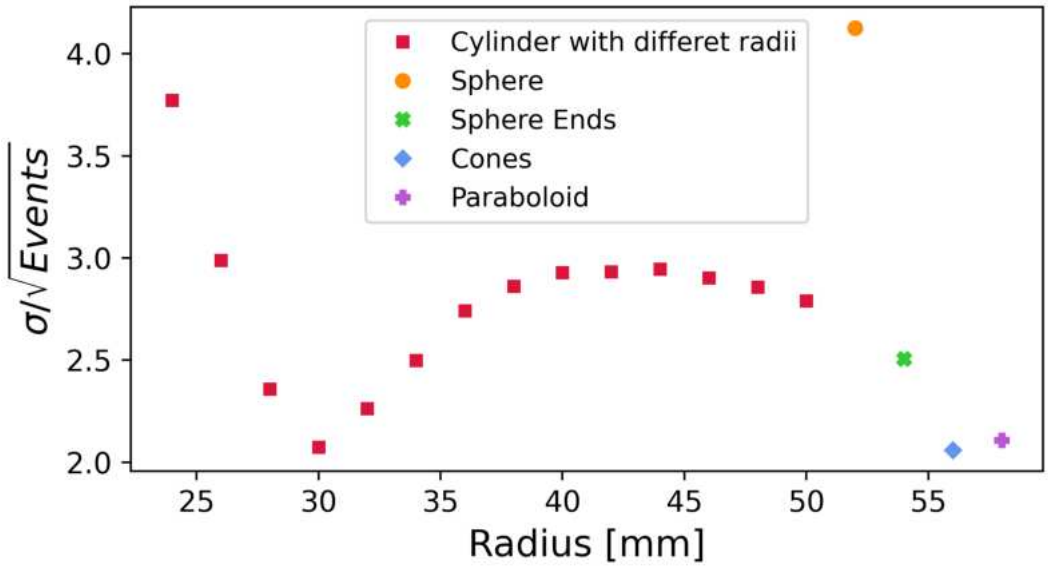

Fig. 4.8.: Standard error of the

the closest to the window cutout radius of $27\,\mathrm{mm}$. From this point on, decreasing the radius will also decrease the statistics, but will not increase the energy resolution. For larger radius, the increase in statistics cannot compensate for the spread of the peak seen in the histogram before. Surprisingly the standard error decreases again for radii larger than $44\,\mathrm{mm}$. Regarding the four differed shapes the cone and paraboloid geometry perform the best. Between these two the paraboiloidal shape was chosen featuring a volume of $550\,\mathrm{mL}$.

For easier manufacturing the inset is split in two. After modelling the geometry in CAD software, the insets were milled from a solid PTFE block by the workshop using a CNC router. The final design of the PTFE insets can be seen in figure 4.9. The additional cutouts and holes ensure a good gas flow and will be explained in the next section.

Fig. 4.9.: Picture of the two insets creating a parapoloidal shape with additional cut outs.

4.4 Loading Strategy

In this section the loading strategy for krypton in LS under pressure is shown. In theory one could also load any kind of gas or liquid with this setup as long as its compatible with the materials. This section is mainly focusing on the gas flow inside the test cell. The piping that leads to the cell is discussed in detail to know why it looks how it looks on the outside as well as on the inside.

For dissolving the Krypton in the LS the idea is to create a sort of bubble column. Letting the gas in at the bottom and letting it out at the top. This bubbling is necessary in order to cut on diffusion time, the time needed in order for the gas to fully saturate the liquid. Without this method one would let the gas in, creating a gas phase and wait for the gas to diffuse through the whole liquid. The typical diffusion constant for example of krypton in water is in the order of magnitude of $10^{-5}\,\mathrm{cm}^2\,\mathrm{s}^{-1}$ [34]. Using this constant one can roughly estimate the time needed in order to saturate the test cell. To get the exact time needed one would have to solve Fick's laws of diffusion but since we only want a rough idea of the time needed we can use the following approximation:

$$< x^2 >= 2 \cdot D \cdot t \tag{4.1}$$

The diameter of the cell is $10\,\mathrm{cm}$ and $11.5\,\mathrm{cm}$ long. Even taking the shortest way, it would take more than 6 days to saturate the whole cell. By bubbling the gas one

introduces convection speeding up the process. Since the two connection pipes are both installed on the same front of the test cell, one pipe needs to extend further into the cell in order to create the bubbling column. The gas enters the cell in through this pipe and for an ideal gas flow the test cell is tilted by an angle of $25°$. This is also where the cutouts in the insets have their role. The two holes going through

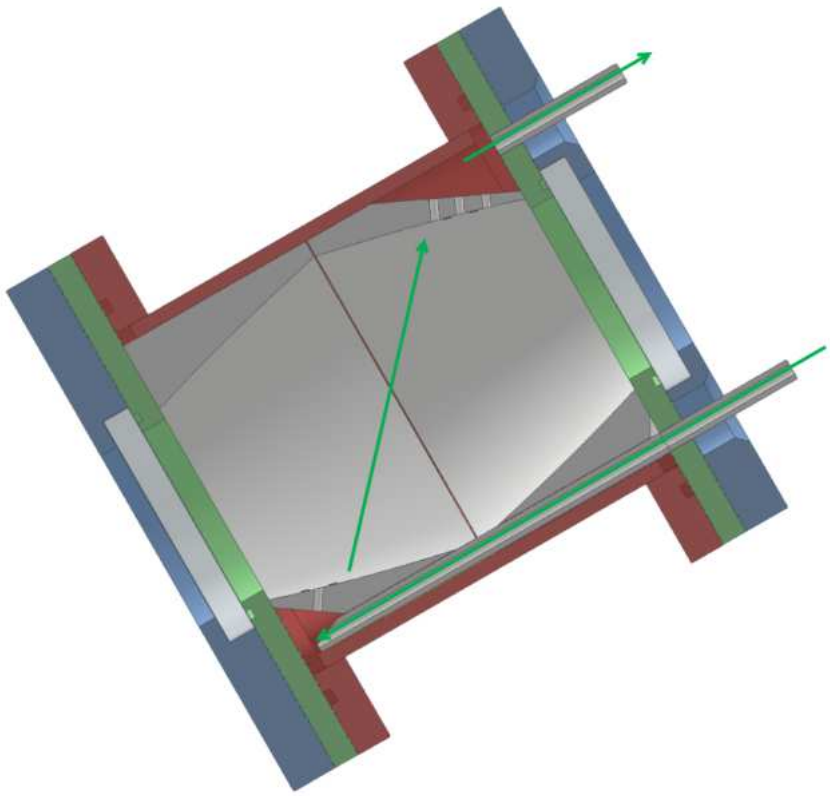

Fig. 4.10.: Half view of the cell model with insets. The gas flow is indicated by the green arrows. The gas is guided to the bottom of the tilted cell trough the pipe extending into the cell here it can bubble through the holes of the insets and then through the LS. At the top a little gas reservoir is create to assure no LS leaves the cell here.

both insets together create a channel for the pipe extending into the cell. Here the gas is inserted in the test cell. The cut out on the lower part as seen in figure 4.10 and the holes in it provide a path for the gas through the insets. Same for the upper cut out. Here also a gas reservoir is created, preventing any liquid being accidentally sucked out and damaging the filling system. This filling system is explained in the following section.

4.5 Krypton Filling System

After discussing the insides of the test cell, this section will take a step away from it and focus on the filling system providing the gas flow and the pressure needed for the loading process. As already seen in figure 4.10, two $6\,\mathrm{mm}$ stainless steel pipes are attached on one side of the cell that can be used for inserting the LS and the krypton. Using a combination of clamp fittings the filling system will include the parts featured in the piping diagram figure 4.11. In the following the idea behind

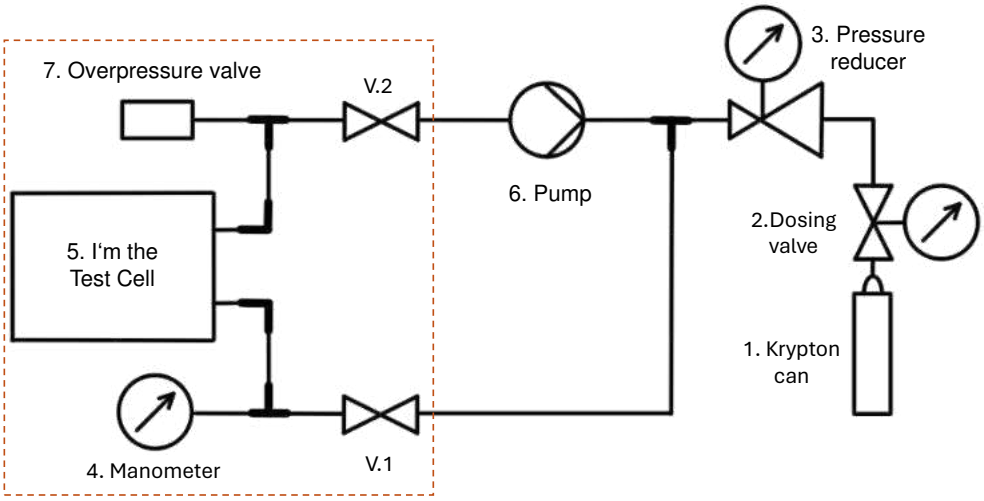

Fig. 4.11.: Sketch of the piping used for loading of krypton in the LS inside the test cell. The parts are discussed in the text. Once the LS is loaded the system can be separated at the two ball valves leaving the parts in the red box that fit into the spectrometer.

this filling system is described. Starting at the krypton bottle 1. with a matching dosing valve 2. including a manometer showing the pressure left in the bottle. This bottle with initially 12 bar is used to generate the pressure in the system. A pressure reducer 3. is used to regulate the pressure of the system behind. The pressure in this part of the filling system is monitored using a manometer 4.. From there the gas is inserted at the bottom pipe of the test cell 5. where it can bubble through the LS as described in section 4.4. Since this dissolving process takes time, a significant amount of gas needs to be bubbled through in order to saturate the hole LS. To avoid wasting this much krypton, it is reused by creating a closed loop. By doing so the gas flow in this system would come to a stop. Therefore a pump (6.) is introduced that cycles the gas without increasing the pressure.

The following list describes the just discussed parts in more detail including the manufacturer and labeling.

- 1. Krypton can, Messer CANgas Aerosol Canisters [35]
- 2. Dosing valve with manometer and hose nozzle, CANgas Armaturenkombi 3
- 3. Pressure reducer
- 4. Manometer, Swagelock PGI-63C-BC9-LASX-B
- 6. Pump, hyco MP65-H5-W14
- V.1,2 Ball valves, Swagelock SS-43GS6MM

Since the realisation of an over pressure valve is not finalised, it is not included in the list. But the idea behind it is to secure the cell from accidentally building up pressure bursting and damaging the integrity of the cell. In addition to those parts, the connections in between, described in the following, are built of a variation of Swagelock and Hy-Lok clamp fittings, both compatible with one another.

- $6\,\mathrm{mm}$ stainless steel piping around $2\,\mathrm{m}$
- Pump adaptors, Hy-Lok CMC6M-4G
- 3x T connectors, Swagelock SS-6M0-3
- 2x L connectors, Swagelock SS-6M0-9

After successfully pressure loading the LS in the test cell the two ball valves V.1 and V.2 can be closed and the piping on the other side of the cell can be detached, indicated with the red box in figure 4.11, leaving the loaded cell with the manometer, over pressure valve and two closing valves. Without the whole filling system the test cell can now fit inside the spectrometer. By making parts of the filling system detachable, the size of the test cell can be maximised, since these parts would have taken space away from the cell.

5 Construction of and Measurements with the Test Cell

> "There is only one thing worse than coming home from the lab to a sink full of dirty dishes, and that is not going to the lab at all!", Chien-Shiung Wu, particle and experimental physicist, Queen of Nuclear Research

This chapter describes the construction of the test cell and the implementation of the infrastructure required to fill the cell with LS and pressurise it with krypton. It explains how the cell itself was assembled and how the first transparency measurements were carried out.

5.1 Building of the Test Cell

After designing the test cell with a CAD program and producing the technical drawings seen in section A.1the steel parts were then fabricated by the local workshop, as were the PTFE insets and the installation of the clamp fittings at the end of each $6\,\mathrm{mm}$ stainless steel pipe. Making sure all the parts fit together, the five stainless steel parts of the cell were assembled, sandwiching the UV-transparent windows in the flanges. The test cell can be seen in figure 5.1b before closing the second flange with the two insets in place. In figure 5.1c the completely closed cell can be seen. At each pipe connector sticking out at the front left and right of the PMT holder in black a corner piece was installed and the additional piping till the valves creating a system that can be completely sealed. To test for leaks one of the two valves was closed and at the other end the compressed air provided in the lab was used to create an over pressure of around $3.8\,\mathrm{bar}$. At this stage, the test cell was not able to hold this pressure for long and some parts have to be reworked to get the desired result. Nevertheless, the working principle of the transparency measurements, which will be discussed in section 5.3, could be tested in this state.

The figure 5.3 shows the arrangement of the pipework up to the two ball valves. The L-connector at the bottom is where the gas enters the cell. This is where the

pressure gauge is attached to keep it in an upright position during loading and when placed inside the spectrometer. From the other connector the pipe goes straight up to prevent any leakage of LS into the filling system. On the input side, this is prevented by bending the tube, as shown in figure 5.3.

5.2 Building of the Test Stand

In addition to the test cell, the measuring infrastructure had to be constructed. This includes the assembly of a rack as seen in figure 5.1a to hold the cell in place while loading and provide a place to measure the loading factor. The frame is made of aluminium profiles, has three levels made of wooden boards and is mounted on four wheels so that it is easy to move around. The top level is used for storing the test cell and is closed on three sides with Plexiglas. The second level of the rack is used to install the pump to avoid the vibration of the pump to influence the loading as little as possible wile still being part of the movable rack. On the lowest level further equipment can be stored.

The top board features four holes which are used to install different kinds of cell holders. To hold the cell in a horizontal position as seen in figure 5.2 a 3D printed holder is used. It is designed to raise the cell from the board providing enough space around the cell for example to install the PMTs as seen in figure 5.1c at each side. With the help of cut outs where the screws of the flange would intersect with the holder, the test cell is prevented from rolling over as well as ensuring the cell is always oriented in the same direction. For the pressure loading of the test cell another holder is used fixing the cell at an angle of $25°$ to the horizontal as can be seen in figure 5.3 also providing a fixed orientation.

5.3 Transparency Measurements

The dimensional requirement of the test cell is to be able to fit into the spectrometer in order to measure the pressure dependent transparency. In figure 5.4 one can see how this goal was achieved. Since the ground plate of the spectrometer is not flat, a little holder was 3D printed to ensure that the cell is placed horizontally parallel to the light path. The red rope around the cell helps to lift the cell in and out of the spectrometer providing a better grip than the round cell itself. The alignment parallel to the light path is adjusted by aligning the side without the pipes with

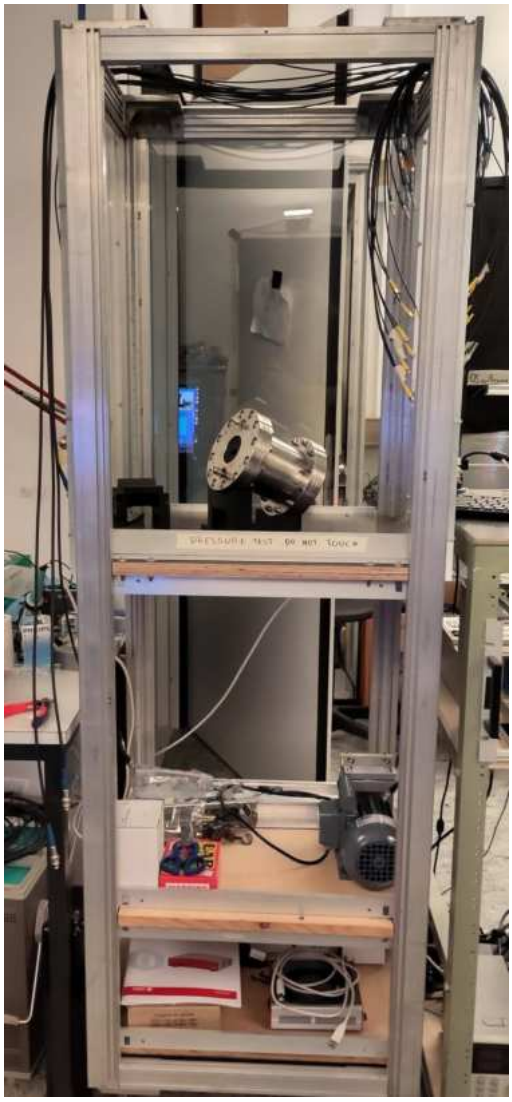

(a) The Rack used to mount the test cell when loading and measuring the loading factor.

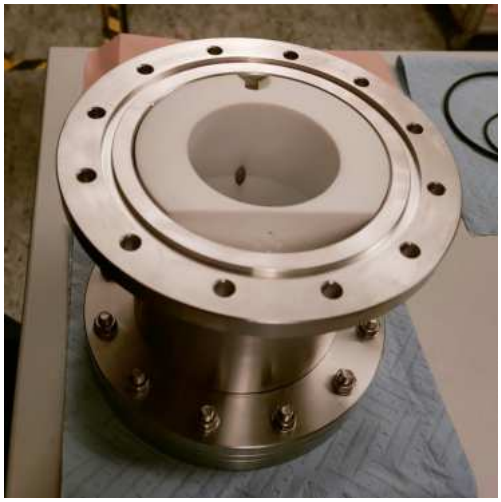

(b) View of the test cell before closing with the insets fitting tightly inside.

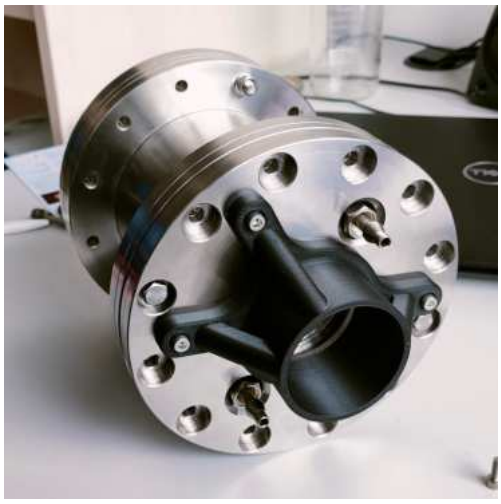

(c) Closed test cell with the PMT holder mounted at the front

Fig. 5.1.: Collection of pictures of a) the Rack and b,c) the test cell in the open and closed state.

the wall of the spectrometer. Since the test cell is not fixed to the frame of the spectrometer like normal cuvettes, it is necessary to see how the test cell performs in transparency measurements and how well those measurements can be reproduced. The empty test cell was probed by doing the same transparency measurement over and over while removing the test cell after every measurement. The spectrometer uses a monochromator to seclect wavelengths between $250\,\mathrm{nm}$ and $600\,\mathrm{nm}$ which is guided through the samples in the light path. The transmitted light, so the light not absorbed by the medium in the light path is then measured. The spectrometer has two light paths that can be used simultaneously, one being the reference for

Fig. 5.2.: Picture of the cell mounted vertically on the rack. On the right side of the cell, at the two pipe connectors, the piping is installed up to the two valves

the other. The idea is to place the test cell in the back light path with the option of placing a reference cell in the front light path.

The results from the empty test cell can be seen in figure 5.5 where the absorbance is plotted against the wavelength. The orange lines represent the just mentioned measurements of the empty test cell, ten in total. For comparison an empty $10\,\mathrm{cm}$ cuvette was also measured which is shown in the green line. Its absorbance is mainly caused by Fresnel effects also present in the windows of the test cell. The offset in absorbance between the test cell and the cuvette for wavelengths greater than $400\,\mathrm{nm}$ comes from the difference in thickness of the $8\,\mathrm{mm}$ thick Plexiglas windows of the cuvette glass. Below $400\,\mathrm{nm}$ the Plexiglas shows the expected increase in absorbance. The blue curve is the result of a intentionally bad placed cell inside the spectrometer, resulting in a visible deviation from the orange curves. By using the empty cell as reference in the second light path of the spectrometer, the purple lines are measured representing the difference of the empty test cell and the cuvette. To test this hypothesis, the difference between the mean of the spectrum and the test cell is calculated resulting in the dotted purple line. Assuming that the Fresnel effect of the test cell and the cuvette result in the same absorbance, the difference between these two lines represent the absorbance of the in total $16\,\mathrm{mm}$ thick Plexiglas The

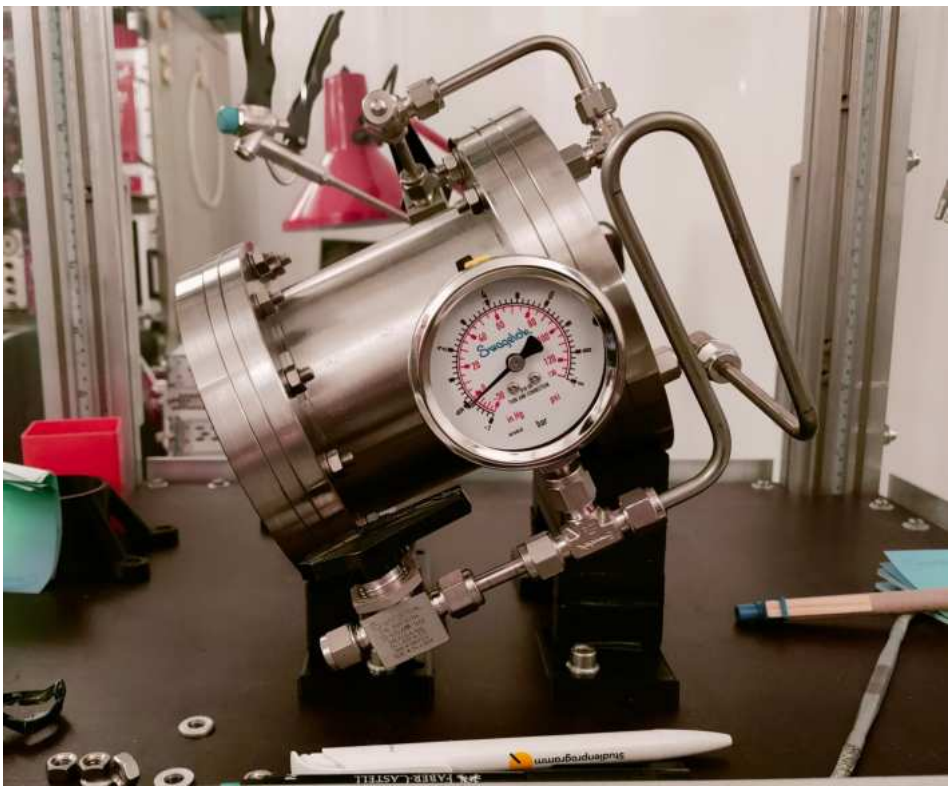

Fig. 5.3.: Picture of the test cell mounted on the tiled holder, which is used for the gas loading of the cell. The pipe connected at the bottom is updated to the first design to avoid liquid flowing back into the filling system.

brown curve in the plot right below shows the relative error of the orange lines from above clearly showing that in the ultraviolet region between $260\,\mathrm{nm}$ and $600\,\mathrm{nm}$ the measurement is more prone to errors. This measurement shows that the test cell functions as expected and intended.

After showing the working principle of the test cell without anything inside, the next step was to fill the cell and see if the test cell is liquid tight, how the filling works and if the transparency measurements are reliable. This was done by using linear alkylbenzenes, in short LAB. Inserted by one of the connecting pipes the whole test cell was filled and then measured in the spectrometer as before. Three different measurements were made using again different combinations of the filled test cell and a $10\,\mathrm{mm}$ cuvette also filled with LAB, and can be seen in figure 5.6. The yellow green and blue curves show the absorbance spectrum of the LAB filled test cell. In purple the same is done with the cuvette. The brown to orange curves show the combination of the test cell with the cuvette as reference, these should represent the difference of cell and cuvette. The dotted black line is not a direct measurement but the calculated difference of the cuvette from the test cell. One can see that for

Fig. 5.4.: View inside the spectrometer with the test cell tightly fitting in the back light path and a cuvette in the front light path. The red rope around the test cell is installed in order to lift the cell in and out of the spectrometer

wavelengths smaller than $280\,\mathrm{nm}$ this curve diverges from the measured data. The reason for this is the maximum absorbance the spectrometer can reach.

One interesting value is the attenuation length λ describing how far the photon can travel in a material until the probability that the photon has not been absorbed drops to 1/e. Since the absorbance measured in the spectrometer includes the absorption of the Plexiglas and Fresnel effects at the window surfaces the data has to be corrected. For the cuvette this is done by subtracting half the absorbance of the empty cuvette. In the empty cuvette the Fresnel effects occure at every surface when entering and exiting the faces, while when filled with liquid with a similar refractive index the Fresnel effects inside the cuvette disappear, therefore only half of the empty cuvette needs to be subtracted. Assuming the same Fresnel effects in Plexiglas as in the cuvette, the same correction can be done here, subtracting half of the empty cuvette. Additionally the absorbance of the Plexiglas needs to be subtracted leaving only the absorbance of the LAB. The absorbance obtained in this way can now be related to attenuation length using Beer's law, which relates the

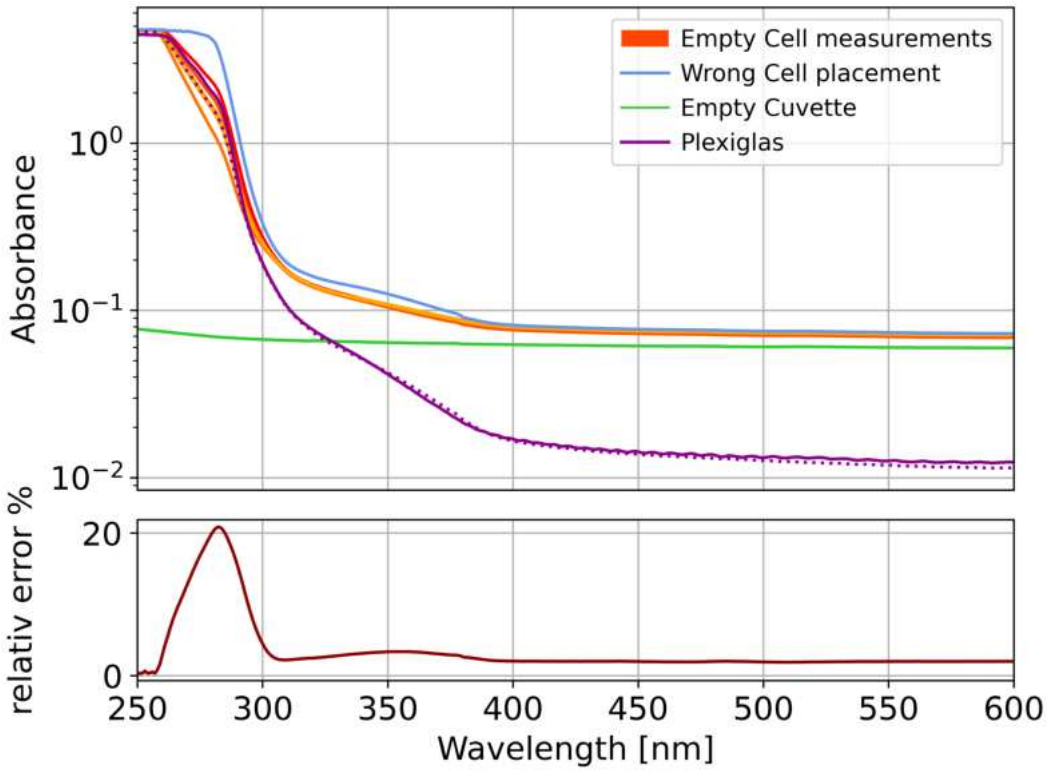

Fig. 5.5.: In orange the absorbance measurement of the empty test cell repeated ten times to look for the reproducibility of this measurement. The blue curve shows an intentionally badly placed cell demonstrating the effects on the absorbance. In green the values for an empty $10\,\mathrm{mm}$ cuvette are shown. The purple curve shows the measurement of the test cell with the cuvette as reference in the second light path of the spectrometer. Here the solid line is the measured value and the dashed line represents the calculated value from subtracting the measurement of the cuvette from the test cell. The plot underneath the absorbance measurements show the relative error of the test cell measurement in orange.

absorbance A to the attenuation length λ and the path length inside the medium d as follows:

$$\lambda = \frac{d}{A \cdot ln(10)} \tag{5.1}$$

With $d = 10\,\mathrm{mm}$ for the cuvette and $d = 12.8\,\mathrm{mm}$ for the test cell, the attenuation length for LAB at $430\,\mathrm{nm}$ is calculated to be $3.38(20)\,\mathrm{m}$ for the cuvette and $3.41(20)\,\mathrm{m}$ in the test cell. To compensate effects of the spectrometer more corrections to the spectrum are normally done but would influence both values in the same way and are therefore not taken into account yet. The measurements show that the cell behaves as intended and that its characteristics are known. Throughout the measurement, no traces of LAB were found on the surfaces beneath the test cell, indicating that it is liquid-tight.

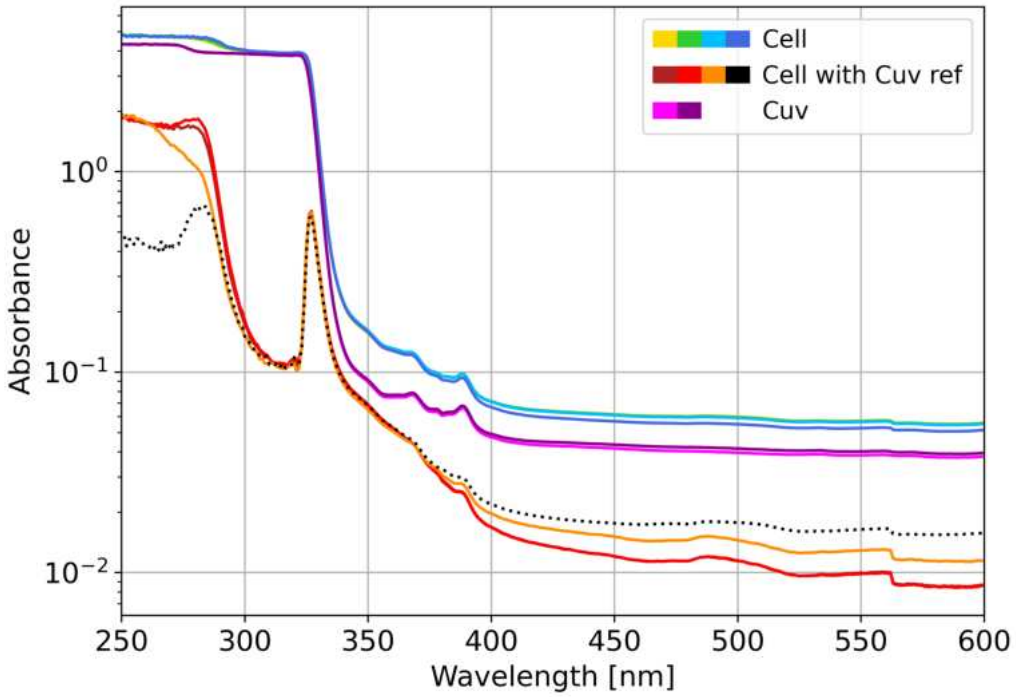

Fig. 5.6.: LAB transparency measurements with the test cell in blue to green. The orange-red curves show the absorbance measurements of the test cell with a LAB filled $10\,\mathrm{mm}$ cuvette as reference in the second light path of the spectrometer. The purple lines show the measurements of this cuvette. The dashed black line shows the calculated value of the cell measurement minus the cuvette values.

6 Sensitivity of the NuDoubt^{++} Detector and OSIRIS

In the context of the proposal for the NuDoubt^{++} experiment, a sensitivity study was performed and is described in this chapter, starting by introducing the signal of the double beta decay and the different backgrounds and how to deal with them before looking at the detector scale needed to be able reach a sensitivity for the measurement of this decay. It will also be discussed how the increase in pressure as described in the sections before can help increase the sensitivity of the detector. The same kind of study can also be performed with other types of detectors showing that with pressure loading also already built scintillator detectors could be upgraded in the search for double beta decay. This will be shown for OSIRIS further explained in the last section.

6.1 Double Beta Signal

The double beta plus isotope ^{78}Kr decays to ^{78}Se via three different decay modes $2\nu 2\beta+$, 2νEC$\beta+$ and 2ν2EC with the expected half-lives as seen in table 6.1. Before the final measurements of $\nu 2\beta++$ decay a the new detector technique needs to be developed by building a prototype still able to measure the normal 2ν decay. The decay mode with the most detection success is the 2νEC$\beta+$ decay mode since compared to the $2\nu 2\beta+$ mode the decay rate is four orders of magnitudes higher. In the 2ν2EC mode the electron which is converted in this process is taken in from the atomic shell leaving an empty space which is filled under the emission of X-rays and Auger electrons. The nuclear binding energy is mostly carried away by neutrinos. With the lack of a positron to identify the decay the only signal which is looked at for this sensitivity study is the 2νEC$\beta+$ mode.

The shape of the signal spectra in this section as well as the following background spectra in section 6.2 was generated using the GEANT4 BxDecay0 C++ library [36].

Tab. 6.1.: Theoretic half-lives for the different decay modes of ^{78}Kr and the current upper detection limit

mode	half-life in years	upper limit in years
2ν2EC	3.7×10^{22}	$>9.2 \times 10^{21}$ [37]
2νEC$\beta+$	5.3×10^{22}	$> 1.1 \times 10^{20}$ [37]
$2\nu2\beta+$	2.3×10^{26}	$>2.0 \times 10^{21}$ [38]

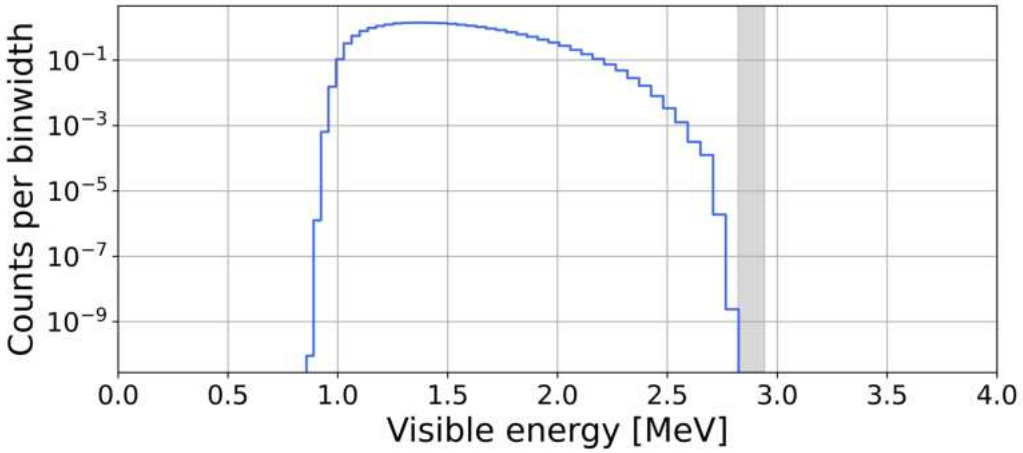

Fig. 6.1.: Normalised spectrum for the 2νEC$\beta+$ decay of ^{78}Kr created using a GEANT4 based simulation. The binning representing the energy resolution of the NuDoubt^{++} detector and energy smeared accordingly. The grey area is the ROI for the neutrinoless double beta decay at $2.881\,\mathrm{MeV}$.

With this extension the decay is simulated without any scintillator quenching or other detector specific properties resulting in a distribution of momentum of the decay particle in p_x, p_y and p_z direction. In total 10^6 decay events where simulated. The visible energy E_{VIS} that a particle can leave in the detector is calculated using equation 6.1 and $m_e = 0.51\,\mathrm{MeV}$.

$$E_{VIS} = \sqrt{m_e^2 + p_x^2 + p_y^2 + p_z^2} - m_e \tag{6.1}$$

For a positron the additional two annihilation gammas adding to the visible energy have to be taken into account as well by adding $2 \cdot m_e$ The binning of the visible energy is chosen to represent the energy resolution of the NuDoubt^{++} detector of $800\,\mathrm{pe/MeV}$ creating the spectrum as seen in figure 6.1. By normalising creating the particle density function (PDF) the spectra can be scaled up and down to represent different modes of pressure, enrichment and half-lives. After taking a look at the relevant backgrounds, in section 6.3 this will be further explained.

6.2 Detector Background

For the search of the double beta decay it is necessary to understand the background. This investigation focuses on processes generating signals in the detector especially in the region of interest (ROI) of the signal seen in figure 6.1 and especially near the Q-value of the neutrinoless case at $2.881\,\mathrm{MeV}$. In the following the two main sources of background will be discussed together with the expected rates for a detector located in a depth comparable to the INFN Gran Sasso National Laboratory (LNGS). These are internal background coming from radioactive decay from isotopes in the detector materials and external backgrounds from the radioactivity from the surrounding including cosmic ray-induced background. A more detailed explanation of the background sources is given in the NuDoubt^{++} proposal [6]

6.2.1 Internal Background

The internal background is mainly caused by impurities of the detector material. The main contributions of radioactive contamination in LAB based scintillators are Uranium and Thorium. Also hard to get rid of is ^{14}C and ^{210}Bi. Due to the handling of the LS with nitrogen also ^{222}Rn is introduced in the detector. In addition to the scintillator, the OWL fibers, used for read out in the NuDoubt^{++} detector, introduce more radioactive particle within the bulk material and especially in form of surface dust. At this stage the contaminations of these fibers are not well known since the production process is not finalised, therefore a conservative estimation for ^{238}U, ^{232}Th, ^{40}K, ^{212}Bi and ^{214}Bi is chosen. The exact values can be found in table 6.2, where all rates are listed together with the produced particles in the decays.

6.2.2 External Background

In addition to the detector itself, radioactivity in the environment of the experiment contributes to the signal in the ROI. Here ^{208}Tl, ^{214}Bi originating from the ^{238}U and ^{232}Th decay chain as well as ^{222}Rn are considered. Some of these are also found in the detector itself mainly the OWL fibers, not adding much to the already high rates here. A big contribution of the cosmic background are high energetic muons. Because the muon is a charged particle just like the electron it also produces Cerenkov and scintillation light in the detector. This can be dealt with by shielding the detector or going underground and install veto detectors. The interactions with the detector creating secondary particles is not so easily detected. Muon initiated

spallation are also an important background especially ^{10}C and ^{11}C where positrons are produced and hard to distinguish from the positron of the $\beta+$ decay of the signal.

6.2.3 Background Rates and Spectrum

Since the location of the detector is not determined yet, the rates used for the sensitivity study are taken from the Borexino experiment [39] located at the LNGS to give a realistic approximation. Most of the gamma rates are higher here because of the introduction of the OWL fibers and also from the wax used in the opaque scintillator. For krypton the rates from other experiments can not be transferred, since in the experiment additional krypton is used instead of minimising the amount. The rate is taken by calculating the amount of krypton atoms as seen in equation 3.1 and using the expected half life converting it to the expected rate. The expected rates can be seen in table 6.2 together with the decay mode which will be relevant for the background disscrimination discussed in the next section 6.3.

Tab. 6.2.: Listing of the Isotopes and the expected rates produncing background in ROI of the spectrum for a the detector located a the LNGS filled with opaque scintillator and OWLs

Element	$\frac{Rate}{tonne \cdot days}$	particle	Element	$\frac{Rate}{tonne \cdot days}$	particle
^{10}C	0.0285	e^+	^{210}Bi	0.39	e^-
^{11}C	0.285	e^+	^{8}B	0.004	e^-
^{14}C	2580	e^-	^{85}Kr	7e8	e^-
^{210}Po	80	α			
Element	$\frac{mBq}{m^3}$	particle	Element	$\frac{mBq}{m^3}$	particle
^{40}K	225	γ	^{214}Bi	2.8	γ
^{60}Co	2.8	γ	^{226}Ra	15.12	γ
^{137}Cs	6	γ	^{228}Th	19.4	γ
^{208}Tl	12	γ	^{232}Th	33.7	γ
^{212}Bi	0.48	γ	^{238}U	103	γ

The spectra for the electron, positron and alpha particles where generated using the same GEANT4 BxDecay0 C++ library [36] as for the signal and is processed in the same way taking the decay particle into concideration with the exeption of ^{8}B. Since this spectrum is nearly flat in the ROI, this spectrum was created using a linear fit of a smaller data set. To generate a data set for the sensitivity study the created spectra where convoluted using a Gaussian distribution with a sigma

according to the energy resolution of each Energy. The so calculated PDFs can be seen in figure 6.2a.

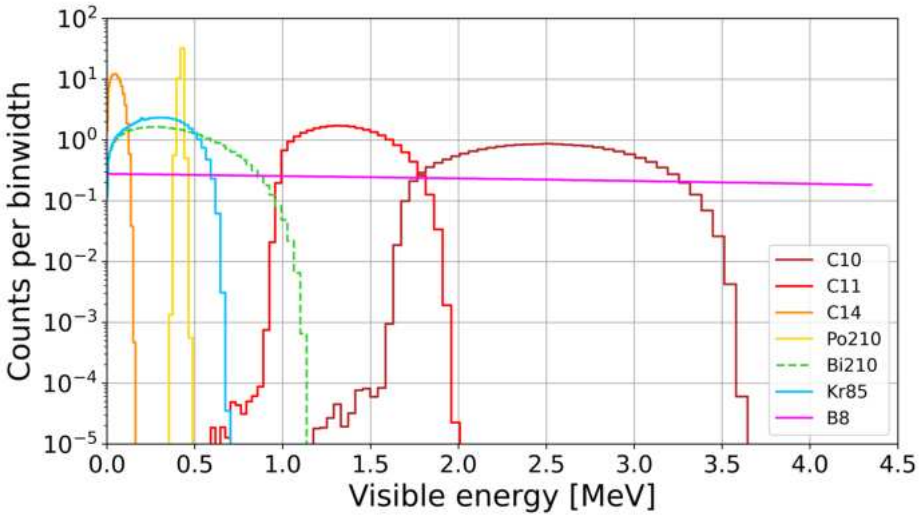

(a)

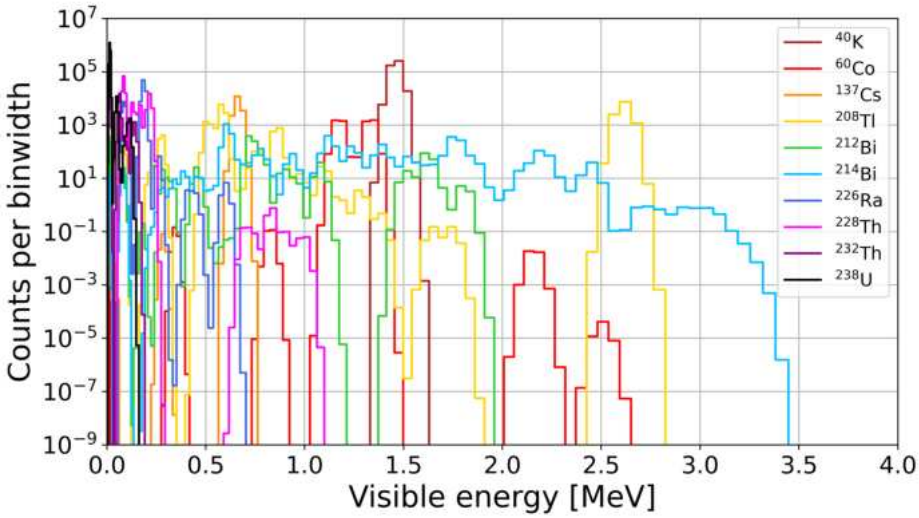

(b)

Fig. 6.2.: Background spectra for the sensitivity study. The binning represents the energy resolution of the NuDoubt^{++} detector of $800\,\mathrm{pe/MeV}$ and is smeared with a Gaussian. a) Normalised background spectrum of electron, positron and alpha particles. b) Gamma spectrum including table 6.2 gamma rates. The sum for each bin is used as one gamma spectrum for future plots.

The energies and intensities, for the gamma decays of each relevant isotope in the background, are taken from the live chart of nuclides [40], excluding any peaks from exited states of the element or any peak without uncertainties. Those peaks were then energy smeared in the same way as for the spectra before and binned in the

same binning. All of them together can be seen in figure 6.2b. Each spectrum was normalised and scaled according to the expected rates from table 6.2. By summing over all spectra for and normalising it again, the total shape of the gamma spectra is created and can be used like the other spectra.

In figure 6.3 the signal can be seen together with the discussed background spectra according tho the expected rates for a detector at the LNGS with natural krypton at normal pressure. One can see that without further background suppression or signal

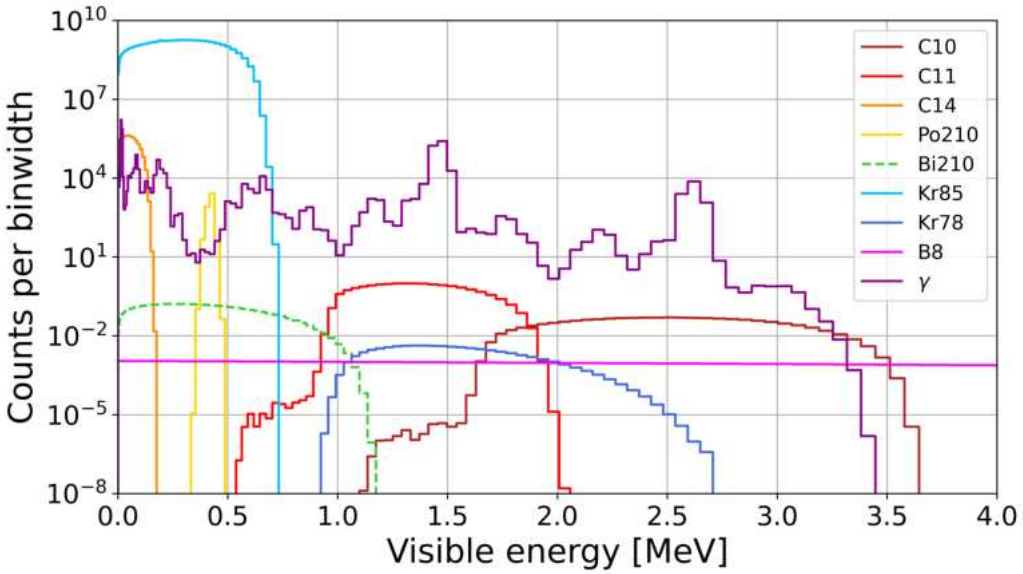

Fig. 6.3.: Spectrum of the backgrounds with the expected rates of table 6.2. In addition the signal of the $2\nu\mathrm{EC}\beta+$ decay in blue.

enhancement the double beta signal, which is more than 4 orders of magnitude lower than the background, is impossible to be distinguished. The strategies to improve this are explained in the next section.

6.3 Improving the signal to background ratio

The first step in improving the background situation is going underground, but as seen in figure 6.3, where this assumption is already applied, further background reduction is necessary. In this section two ways of improvement are elaborated. The first idea is including the event information and looking into particle identification. In addition to this a second idea is increasing the loading pressure.

6.3.1 Background Discrimination

The centerpiece of the NuDoubt^{++} proposal lies in the particle identification power which provides a unique way of discrimination as already described in the theoretical background 2.3. By combining the information of scintillation and Cerenkov light, together with the topology possibilities forming in the opaque scintillator, different particles can be distinguished. The signal consists of positrons creating more scintillation to Cerenkov light than an electron of equal energy. Also the gammas create different patterns in the detector. With this a discrimination power of at least 100 can be applied to the electron and gamma spectra which is still a conservative estimate. For the positron emitting ^{10}C and ^{11}C this is not possible since they produce the same signal as the expected signal. Here the other ways are needed for example including secondary particles of these processes. Therefore the rates of ^{10}C and ^{11}C are only reduced by a factor of 20 and 10. This reduces the initial 4 orders of magnitude to 2 with need for improvement.

6.3.2 Signal Enhancement

The second idea, which is the objective of this master thesis, is the loading of krypton with pressure, increasing the amount of the double beta isotope ^{78}Kr inside the detector, resulting in a higher signal rate. According to Henry's law the amount of krypton dissolved in the scintillator rises linear with pressure which can be seen in figure 6.4. The background reduced by a factor of 100 can be seen as grey lines.

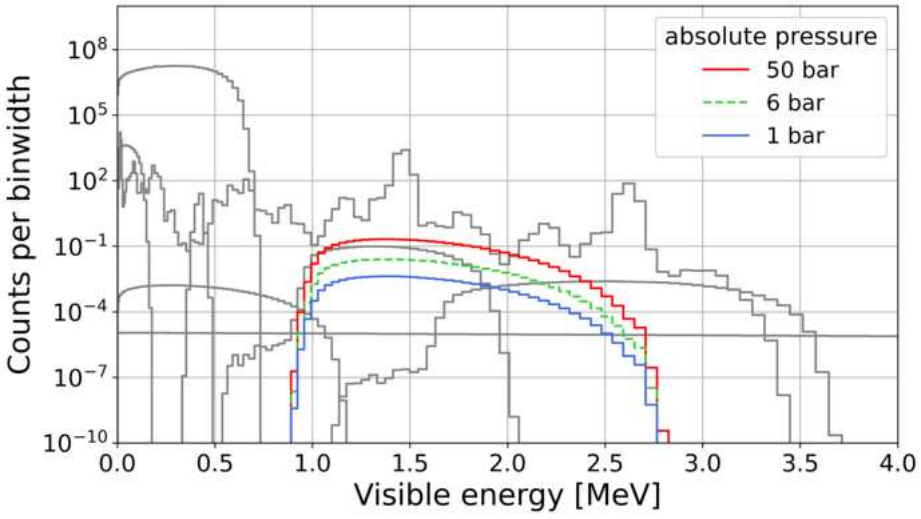

Fig. 6.4.: Expected 2νEC$\beta+$ signal at different loading pressures. In grey the background spectra with a discrimination factor as discussed in the text.

With the background as reference, the coloured lines represent the expected signal spectra for different loading pressures.

One can see that with the reduction and the five bar over pressure the signal is at the same level as the carbons ^{10}C and ^{11}C, unfortunately the gamma spectrum is still more dominant and it would need more than 50 bar over pressure with this technique in order to see the signal against the background.

To avoid having to build a vessel that can hold this much pressure, another method of increasing the amount of double beta isotope ^{78}Kr can be used. In natural krypton the isotope ratio of ^{78}Kr is $0.35\,\%$. By enriching this isotope to for example $50\,\%$ the amount of ^{78}Kr is increased by a factor >100. The question arising from this is what is a good combination of enrichment and pressure loading. The result of both methods is the increase of ^{78}Kr isotopes per volume or detector mass. This is shown in figure 6.5. Here the same discrimination factor is applied on the background

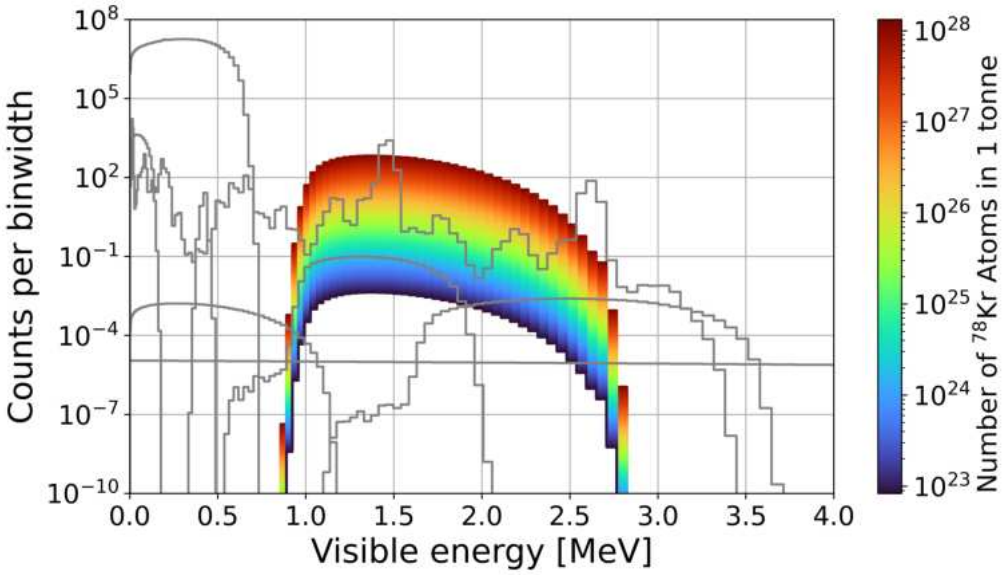

Fig. 6.5.: Expected 2νEC$\beta+$ signal depended on the amount of ^{78}Kr isotope in one tonne of LS. In grey the background spectra with a discrimination factor as discussed in the text.

shown in grey. The colourful lines represent the different amount of ^{78}Kr isotope needed in one tonne of detector to generate this signal. Each line therefore also represents a combination of pressure and enrichment forming the gradient that can be seen in the plot. For reference the natural amount of ^{78}Kr isotope in one tonne of LS is 8×10^{22}.

How the desired amount of ^{78}Kr atoms is reached depends on the detector design. Since enriching krypton is expensive finding a healthy compromise between pressure

loading and enrichment needs to be found. To find the exact amount for a reliable detection of the double beta decay the sensitivity of the NuDoubt^{++} is calculated in the following section.

6.4 Sensitivity calculations

The Sensitivity calculations are based on the background-only hypothesis, finding the rate necessary to say that the signal in the data can not be explained by the background only. In this section the function used for the fit is explained and then used to calculate the sensitivity of the NuDoubt^{++} detector. In the last part, the same method is used for OSIRIS, in order to see if pressure loading is also a suitable way for already existing detectors.

6.4.1 Fit Method

To calculate the sensitivity of the NuDoubt^{++} detector a fit function was developed and is described in the following. The fit is based on a likelihood approach that compares a data set to an expected model and gives a probability of how likely those values are to represent the model. For each bin in the spectrum, the likelihood is evaluated using the Poisson probability $P_\lambda(k)$, where k is the counts in the model bin and λ is the counts from the data. Due to the low rates, Gaussian statistics cannot be applied. As the name log likelihood suggests, the sum of the logarithms, as described in equation 6.2, provides information about how well the assumed values fit the model.

$$-2LLH = \sum -2(log\,(P_\lambda(k))) = -2\sum log\left(\frac{\lambda^k}{k!}\,\mathrm{e}^{-\lambda}\right) \tag{6.2}$$

The problem with Poisson's probability is that it is only defined for integer values of k. To solve this problem, the Stirling's approximation $\ln(k!) = k\ln k - k$ is introduced resulting in:

$$-2LLH = \sum -2(log(\lambda)k - log(k)k + k - \lambda) \tag{6.3}$$

To find the best parameter for the data set to fit the model this function is evaluated using the minimize function of scipy.optimize.minimize [41].

6.4.2 Sensitivity Results of the NuDoubt^{++} Detector

For the NuDoubt^{++} detector the spectra and rates are used as already explained above in this chapter including the background discrimination factor of 100 for gammas, electrons and alpha particles and 20 and 10 for ^{10}C and ^{11}C. For the fit a set of data is created including all the background spectra and the signal with different rates. For each the background is fitted using the -2LLH function (equation 6.3). This was not only done with different signal rates but also for different run times of the detector. A longer run time increases the statistics thus lower signal rates are needed be able to detect them. Because no self shielding of the detector volume is assumed, the same scaling can be done with the detector size. The behavior of the -2LLH results can be seen in figure 6.6.

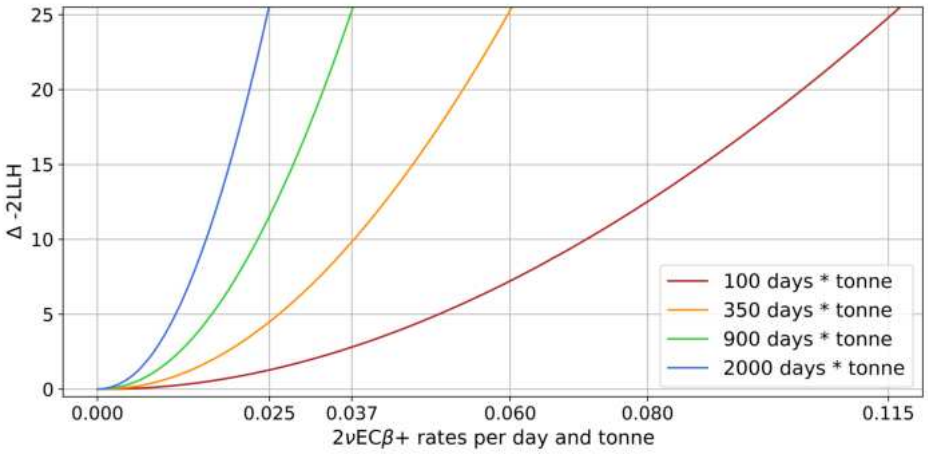

Fig. 6.6.: -2 Log Likelihood profile of the fit for the NuDoubt $^{++}$ detector. Different curves representing different combination of run time and detector volume.

The minimal rate needed for a 5σ discovery is taken from the curve where the -2LLH has changes by a value of 25 from the minimal value. With the number of ^{78}Kr atoms N in one tonne of detector. The shorter the half-life the higher their decay rate and fewer atoms are needed to reach the given half-life. This minimum rate can be translated into a half life by using:

$$t_{1/2} = \frac{ln(2) \cdot N}{rate} \tag{6.4}$$

This behavior can be seen in the final sensitivity plot, figure 6.7a. The solid coloured lines represent the different rates from figure 6.6 showing the relation from equation 6.4. The lines show the upper limit of the half-lives that could be detected. Everything under the curve is detectable.

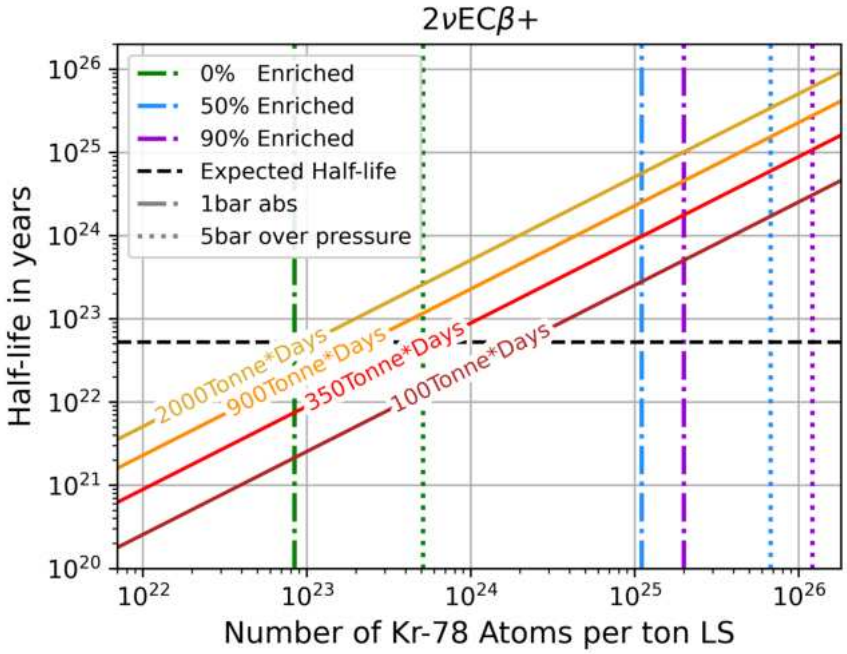

(a)

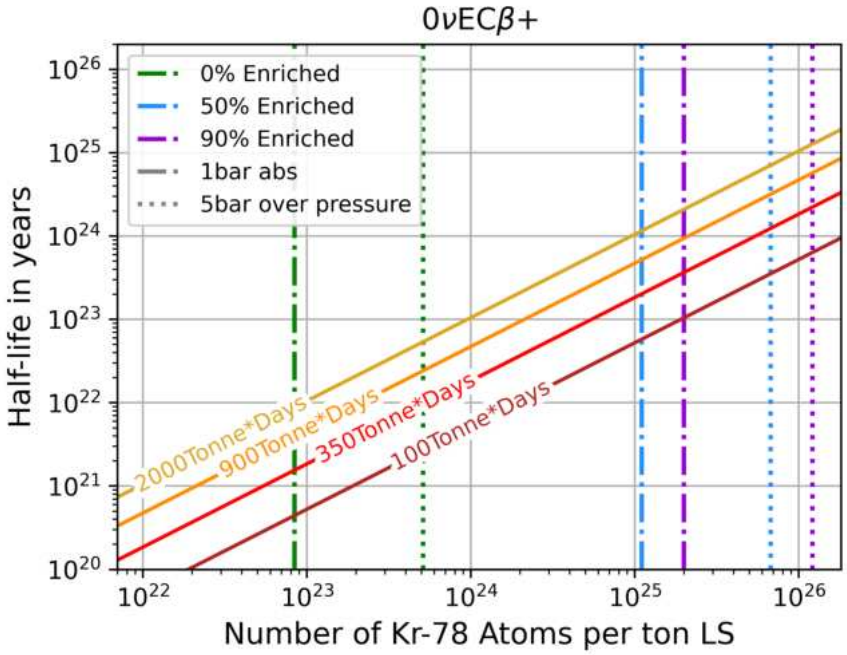

(b)

Fig. 6.7.: Results of the sensitivity study for the NuDoubt^{++} detector. Vertical lines represent different enrichment and loading pressures. The horizontal dashed line shows the expected half life. Sanded lines represent a) the sensitivity of the NuDoubt^{++} detector on the measurement of the 2νEC$\beta+$ decay calculated form the minimal decay rate needed for the background only fit to fail (5σ) explaining the data including a signal of a certain rate. b) the exclusion sensitivity of the NuDoubt^{++} detector on the 0νEC$\beta+$ measurement(90%CL). Both show the value for different combinations of run time and detector volume

The vertical lines represent different loading factors and enrichment cases. In green natural krypton is used, for the blue and purple line 50% and 90% enriched ^{78}Kr is assumed. Also shown in the form of different line styles is the effect of pressure loading comparing normal pressure to $5\,\mathrm{bar}$ over pressure. To visualise the goal of this stage of the experiment, the theoretical value of the $2\nu\mathrm{EC}\beta+$ decay of $5.3 \times 10^{22}\,\mathrm{years}$ is added in the form of a horizontal dashed line. It can be seen that without enriching the ^{78}Kr and or pressure loading, the goal of measuring the double beta decay can not be achieved without extensive run time. Dependent on the run time of the experiment, a minimal amount of 10^{24} ^{78}Kr per tonne LS is needed. Note that the effect of a longer run time and larger detector volume scales with the square root of the number of decays, giving a smaller increase in sensitivity as more is measured.

The same procedure can also be made for the neutrinoless case, only looking at the 2σ region around $2.881\,\mathrm{MeV}$ as seen in figure 6.3 where the ROI is shown in grey. To account for the energy resolution of the detector the ideally mono energetic energy is also smeared with a Gaussian like the background spectra. The data is generated by using the background rates in the ROI. On this data the background rates are fitted together with a fixed amount of signal. This results in a -2LLH profile like already seen in figure 6.6. To get the exclusion sensitivity the -2LLH profile is evaluated at the 90% confidence interval giving back the smallest signal rate needed to deviate from the hypothesis of no signal in the data. This rate is prepared in the same way which can be seen in figure 6.7b. One can see that with the current conservative techniques only an upper limit on the neutrinoless case can be made, which still is better than the current upper limit of $1.1 \times 10^{20}\,\mathrm{years}$.

6.4.3 Sensitivity Results of OSIRIS

To see if the loading of already existing scintillator detectors with krypton results in the possibility of measuring a double beta decay, the same sensitivity study is transferred to the Online Scintillator Internal Radioactivity Investigation System, in short OSIRIS. A detector located in southern china next to the medium baseline reactor neutrino experiment JUNO. OSIRIS is the detector analysing the radio purity of the LS used in JUNO. After measuring the mass hierarchy in the neutrino mass in JUNO, the OSIRIS detector can be used for other measurements like the double beta decay.

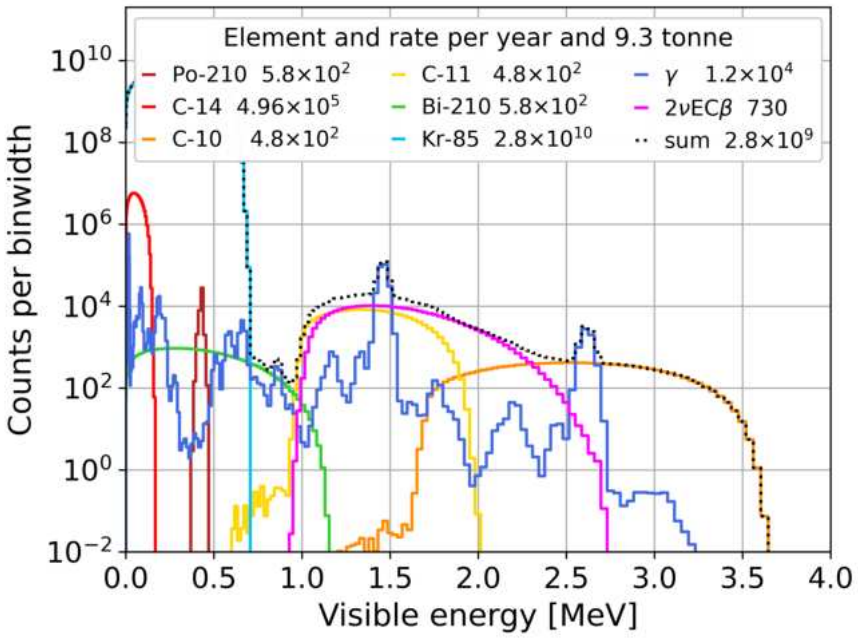

(a)

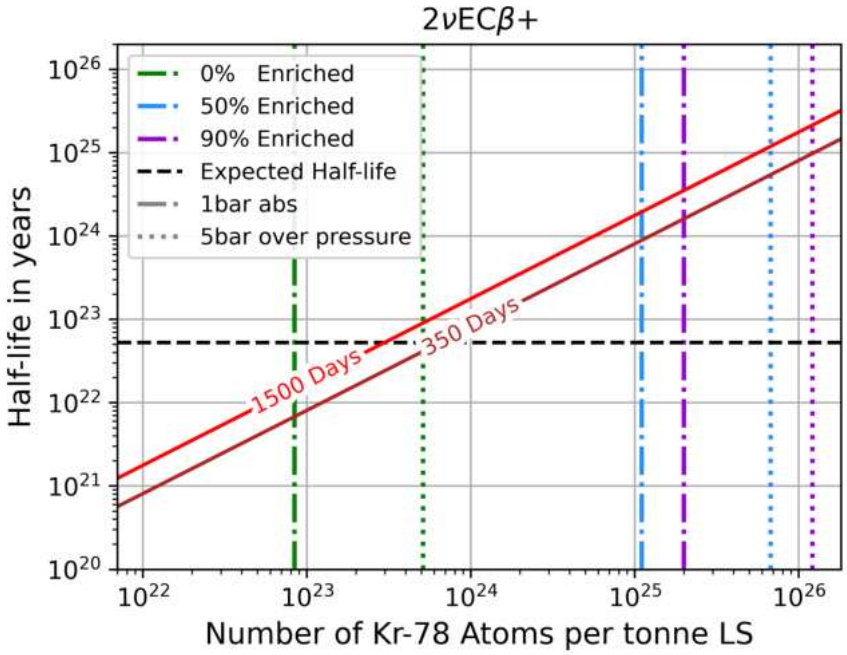

(b)

Fig. 6.8.: a) Expected rates for a run time of one year using a loading pressure of $5\,\mathrm{bar}$ and 50% enriched ^{85}Kr in OSIRIS. b) Result of the sensitivity study. Vertical lines represent different enrichment and loading pressures. The horizontal dashed line shows the expected half life. Sanded lines represent sensitivity of OSIRIS on the measurement of the $2\nu\mathrm{EC}\beta+$ decay calculated form the minimal decay rate needed for the background only fit to fail (5σ) explaining the data including a signal of a certain rate. This is shown for two differed run times.

The fiducial volume of the OSIRIS detector is $9.3\,\mathrm{tonne}$, using the rates from [42] the background spectrum can be created in using the same spectra generated for the NuDoubt^{++} experiment only scaling them up as needed. This can be seen in figure 6.8a with the expected rates of each element in the fiducial volume over one year. Here also the double beta signal can be seen in the case of 50% enriched ^{78}Kr loaded with $5\,\mathrm{bar}$. One can see that the gamma spectrum is lower than in the NuDoubt^{++} experiment, because without the introduction of the OWL fibres and therefore without the surface dust the radio purity of the detector is much higher, leaving the ^{10}C and ^{11}C as main background. Since the OSIRIS upgrade with an energy resolution of 2000 pe/MeV is higher than the NuDoubt^{++} detector the binning is also adapted as well as the energy smearing.

With these spectra the same fit procedure is made resulting in the already established sensitivity plot figure 6.8b featuring the sensitivity of a run time of roughly one and four years. Without any further background discrimination the minimal amount of ^{78}Kr atoms per tonne LS is in the order of 10^{24}. These results show a similar sensitivity on the double beta decay as the NuDoubt^{++} detector but uses a larger volume, useful for self shielding and statistics but rises the amount of Krypton needed.

7 Conclusion and Outlook

> "What we know is really very, very little compared to what we still have to know.", Fabiola Gianotti, experimental particle physicist and first woman Director-General at CERN

The measurement of the rare double beta decay is key for developing methods for the measurement of the even rarer neutrinoless double beta decay and the of physics beyond the SM. The NuDoubt^{++} experiment offers new opportunities introducing advanced scintillator and the necessary background reduction techniques. Existing detectors like OSIRIS that already have low background rates are also interesting candidates for double beta experiments.

In the scope of this thesis the potential of these two detectors are shown using conservative assumptions of background discrimination and energy resolution. The results of this sensitivity study show that in both detectors the measurement of the double beta decay is only possible if a certain rate of double beta isotope is present in the detector ensuring a higher signal than background rates. The amount of krypton, 10^{24} ^{78}Kr atoms per tonne LS, is on the same order of magnitude for both detectors but for OSIRIS this needs to be implemented in the whole $9.3\,\mathrm{tonne}$ volume adding one order of magnitude. The size of the NuDoubt^{++} is not finalised and the full potential of background discrimination is not implemented in the study. With further elaboration and fine tuning of the techniques used in the NuDoubt^{++} detector, this experiment stands out as a promising candidate to providing one of the first measurements of the neutrinoless double beta plus decay. For both detectors it is essential to reduce the cosmogenic ^{10}C and ^{11}C background either by going deeper underground or with more elaborate discrimination techniques i.e. including secondary particles.

In the scope of this thesis the first step of understanding the pressure loading needed for such experiments is made. A small scale overpressure test cell can be used to work out the necessary techniques. The design of this test cell is motivated by the requirements to be able not only to load LS with krypton but also to measure how much the krypton concentration increases with pressure and also to measure the scintillation and transparency properties of it. The size and material of the cell is optimised by simulating the ^{85}Kr decay which will be used for measuring the total

amount of Krypton in the LS. The absorbance measurements with test cell showed the behaviour of the Plexiglas window as expected. This made it possible to measure a LAB sample and obtain the same result in the test cell as in a traditional cuvette. Although no liquid leaking, the test cell is not sufficiently pressure tight yet. Here further analysis on the parts is needed in order to identify the gas leaks, which might result in rebuilding some parts of the test cell for a tighter fit. In order to measure the exact loading factor, it is necessary to know the activity of the krypton. This could be done by using a proportional counting cell.

In summary, this thesis demonstrates the advantages of pressure loading in the search for the neutrinoless double beta decay and takes the first steps towards understanding how this could be used.

Bibliography

[1] T. Wester, K. Abe, C. Bronner, et al. “Atmospheric neutrino oscillation analysis with neutron tagging and an expanded fiducial volume in Super-Kamiokande I–V”. In: *Physical Review D* 109.7 (Apr. 2024) (cit. on p. 1).

[2] Q. R. Ahmad, R. C. Allen, T. C. Andersen, et al. “Measurement of the rate of nu_e + d –> p + p + e⁻ interactions produced by 8B solar neutrinos at the Sudbury Neutrino Observatory”. In: *Physical Review Letters* 87.7 (July 2001) (cit. on p. 1).

[3] Frank T. Avignone, Steven R. Elliott, and Jonathan Engel. “Double beta decay, Majorana neutrinos, and neutrino mass”. In: *Rev. Mod. Phys.* 80 (2 Apr. 2008), pp. 481–516 (cit. on p. 1).

[4] S. Abe, S. Asami, M. Eizuka, et al. “Search for the Majorana Nature of Neutrinos in the Inverted Mass Ordering Region with KamLAND-Zen”. In: *Phys. Rev. Lett.* 130 (5 Jan. 2023), p. 051801 (cit. on pp. 1, 7).

[5] M. Agostini, G. R. Araujo, A. M. Bakalyarov, et al. “Final Results of GERDA on the Search for Neutrinoless Double-β Decay”. In: *Phys. Rev. Lett.* 125 (25 Dec. 2020), p. 252502 (cit. on p. 1).

[6] Sebastian Böser, Stefan Schoppmann, Alfons Weber, and Michael Wurm. “(working title)Combining Hybrid and Opaque Scintillator Techniques in Search for Double Beta Plus Decays. A Concept Study for the NuDoubt++ Experiment”. In: (2024). not yet published (cit. on pp. 1, 7, 43).

[7] A. Gando, Y. Gando, H. Hanakago, et al. “Measurement of the double-β decay half-life of ^{136}Xe with the KamLAND-Zen experiment”. In: *Phys. Rev. C* 85 (4 Apr. 2012), p. 045504 (cit. on p. 1).

[8] Kai Zuber. *Neutrino Physics*. Taylor and Francis, 2020 (cit. on p. 3).

[9] Wolfgang Pauli. “Pauli letter collection: letter to Lise Meitner”. Typed copy (cit. on p. 3).

[10] C. L. Cowan, F. Reines, F. B. Harrison, H. W. Kruse, and A. D. McGuire. “Detection of the Free Neutrino: a Confirmation”. In: *Science* 124.3212 (1956), pp. 103–104. eprint: `https://www.science.org/doi/pdf/10.1126/science.124.3212.103` (cit. on p. 3).

[11] G. Danby, J-M. Gaillard, K. Goulianos, et al. “Observation of High-Energy Neutrino Reactions and the Existence of Two Kinds of Neutrinos”. In: *Phys. Rev. Lett.* 9 (1 July 1962), pp. 36–44 (cit. on p. 3).

[12] K. Kodama, N. Ushida, C. Andreopoulos, et al. “Observation of tau neutrino interactions”. In: *Physics Letters B* 504.3 (2001), pp. 218–224 (cit. on p. 3).

[13] Bruce T. Cleveland, Timothy Daily, Jr. Raymond Davis, et al. “Measurement of the Solar Electron Neutrino Flux with the Homestake Chlorine Detector”. In: *The Astrophysical Journal* 496.1 (Mar. 1998), p. 505 (cit. on p. 3).

[14] Q. R. Ahmad, R. C. Allen, T. C. Andersen, et al. “Measurement of the Rate of $\nu_e + d \rightarrow p + p + e^-$ Interactions Produced by ^8B Solar Neutrinos at the Sudbury Neutrino Observatory”. In: *Phys. Rev. Lett.* 87 (7 July 2001), p. 071301 (cit. on p. 3).

[15] M Aker, M Balzer, D Batzler, et al. “KATRIN: status and prospects for the neutrino mass and beyond”. In: *Journal of Physics G: Nuclear and Particle Physics* 49.10 (Sept. 2022), p. 100501 (cit. on p. 4).

[16] Wikimedia Commons. *Doppelbeta-massenparabel.png — Wikimedia Commons, the free media repository*. [Online; accessed 09-mai-2024]. 2024 (cit. on p. 4).

[17] Giovanni Benato. “Measurement of two neutrino double beta decay with the LArGe facility at Gran Sasso”. PhD thesis. Sept. 2011 (cit. on p. 5).

[18] Ettore Majoran. “A SYMMETRIC THEORY OF ELECTRONS AND POSITRONS”. In: *l Nuovo Cimento* 14 (1937), pp. 171–184 (cit. on p. 5).

[19] Guofu Cao. “Search for $0\nu\beta\beta$ decay with EXO-200 and nEXO”. In: *PoS* HQL2018 (2018), p. 054 (cit. on p. 6).

[20] Giovanni Benato. “Effective Majorana mass and neutrinoless double beta decay”. In: *The European Physical Journal C* 75.11 (Nov. 2015) (cit. on p. 6).

[21] Glenn F Knoll. *Radiation detection and measurement; 4th ed.* New York, NY: Wiley, 2010 (cit. on p. 7).

[22] Wikimedia Commons. *File:Franck-Condon-Prinzip.svg — Wikimedia Commons, the free media repository*. [Online; accessed 09-mai-2024]. 2024 (cit. on p. 8).

[23] *Equilibrium Thermodynamics*. [Online; accessed 9-mai-2024] (cit. on p. 9).

[24] František Cejnar, Ludmila Wilhelmová, and Pavel Vrzala. “Noble gas solubility measurement in liquid scintillator solvents”. In: *The International Journal of Applied Radiation and Isotopes* 28.3 (1977), pp. 281–284 (cit. on pp. 11, 12).

[25] H.L. Clever. *Krypton, Xenon & Radon*. IUPAC Solubility Data Series. Elsevier Science, 2013 (cit. on p. 11).

[26] A. Gando, Y. Gando, H. Hanakago, et al. “Measurement of the double-β decay half-life of ^{136}Xe with the KamLAND-Zen experiment”. In: *Physical Review C* 85.4 (Apr. 2012) (cit. on p. 12).

[27] Y. Gando, A. Gando, T. Hachiya, et al. “The nylon balloon for xenon loaded liquid scintillator in KamLAND-Zen 800 neutrinoless double-beta decay search experiment”. In: *Journal of Instrumentation* 16.08 (Aug. 2021), P08023 (cit. on p. 12).

[28] William M Smethie and Guy Mathieu. “Measurement of krypton-85 in the ocean”. In: *Marine Chemistry* 18.1 (1986), pp. 17–33 (cit. on p. 13).

[29] Francis J. Norton. “Krypton Diffusion in Scintillation Counter Plastic”. In: *nature* 218.5137 (Apr. 1968), p. 165 (cit. on p. 13).

[30]Balraj Singh and Jun Chen. “Nuclear Data Sheets for A = 85”. In: *Nuclear Data Sheets* 116 (Feb. 2014), pp. 1–162 (cit. on p. 13).

[31]Perkin Elmer. *LAMBDA 650/850/950*. 2004. URL: https://cmdis.rpi.edu/sites/default/files/UVVis-PerkinElmer-Lambda950-HardwareGuide.pdf (visited on Nov. 21, 2013) (cit. on pp. 14, 15).

[32]M. Rubel, G. De Temmerman, J. Coad, et al. “Mirror test for International Thermonuclear Experimental Reactor at the JET tokamak: An overview of the program”. In: *Review of Scientific Instruments* 77 (June 2006) (cit. on p. 20).

[33]J. Alt, O. Bezshyyko, M. Böhles, et al. *Performance of a First Full-Size WOM-Based Liquid Scintillator Detector Cell as Prototype for the SHiP Surrounding Background Tagger*. 2024. arXiv: 2311.07340 [physics.ins-det] (cit. on p. 22).

[34]D.L. Wise and G. Houghton. “Diffusion coefficients of neon, krypton, xenon, carbon monoxide and nitric oxide in water at 10–60°C”. In: *Chemical Engineering Science* 23.10 (1968), pp. 1211–1216 (cit. on p. 28).

[35]Messer Schweiz AG. *CANgas*. https://specialtygases.messergroup.com/de/druckdosen. last accesed: 2024 (cit. on p. 31).

[36]Volodymyr Tretyak François Mauger. *BxDecay0*. https://github.com/BxCppDev/bxdecay0. 2023 (cit. on pp. 41, 44).

[37]Yu. M. Gavrilyuk, A. M. Gangapshev, V. V. Kazalov, et al. “Indications of $2\nu 2K$ capture in ^{78}Kr”. In: *Phys. Rev. C* 87 (3 Mar. 2013), p. 035501 (cit. on p. 42).

[38]C. Sáenz, E. Cerezo, E. García, et al. “Results of a search for double positron decay and electron-positron conversion of ^{78}Kr”. In: *Phys. Rev. C* 50 (2 Aug. 1994), pp. 1170–1174 (cit. on p. 42).

[39]G. Bellini, J. Benziger, D. Bick, et al. “Final results of Borexino Phase-I on low-energy solar neutrino spectroscopy”. In: *Phys. Rev. D* 89 (11 June 2014), p. 112007 (cit. on p. 44).

[40]International Atomic Energy Agency - Nuclear Data Section. *Live Chart of Nuclides*. https://www-nds.iaea.org/relnsd/vcharthtml/VChartHTML.html. Apr. 2024 (cit. on p. 45).

[41]Pauli Virtanen, Ralf Gommers, Travis E. Oliphant, et al. “SciPy 1.0: Fundamental Algorithms for Scientific Computing in Python”. In: *Nature Methods* 17 (2020), pp. 261–272 (cit. on p. 49).

[42]Lukas Bieger, Thilo Birkenfeld, David Blum, et al. “Potential for a precision measurement of solar pp neutrinos in the Serappis experiment”. In: *The European Physical Journal C* 82.9 (Sept. 2022) (cit. on p. 54).

Appendix

A

A.1 Technical drawings of the Test Cell

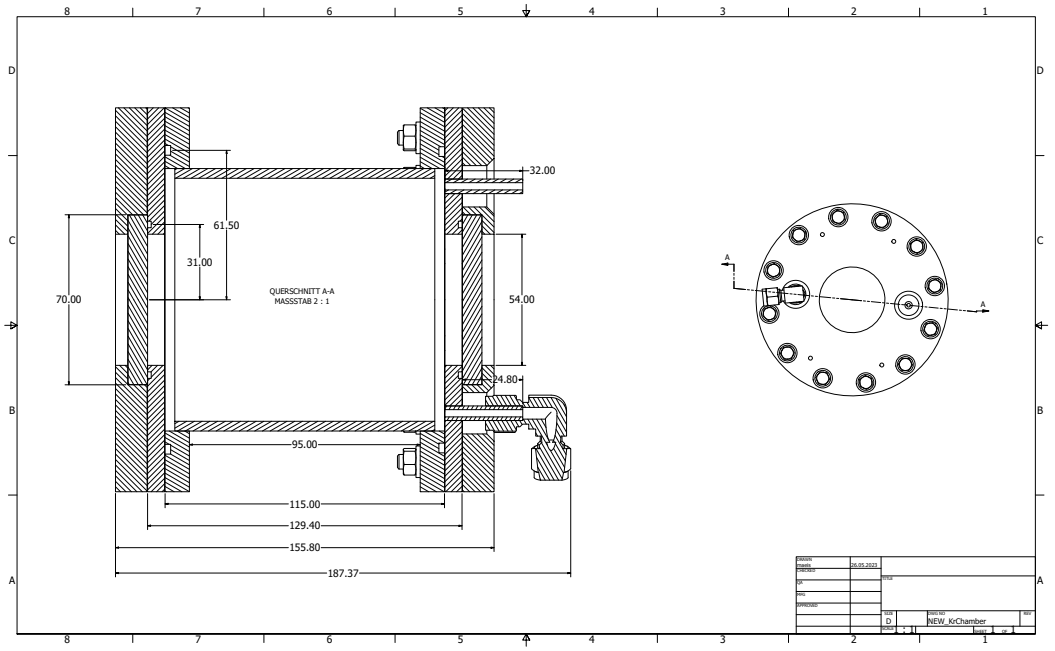

Fig. A.1.: Overview of the test cell with dimensions including estimates for additional spacing from the o-rings

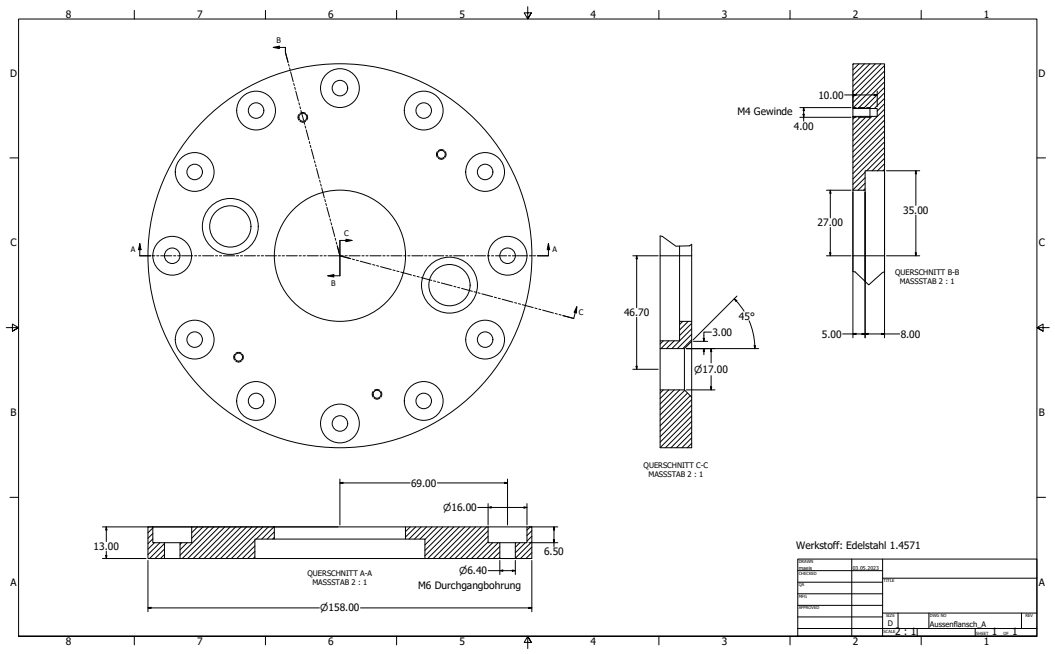

(a)

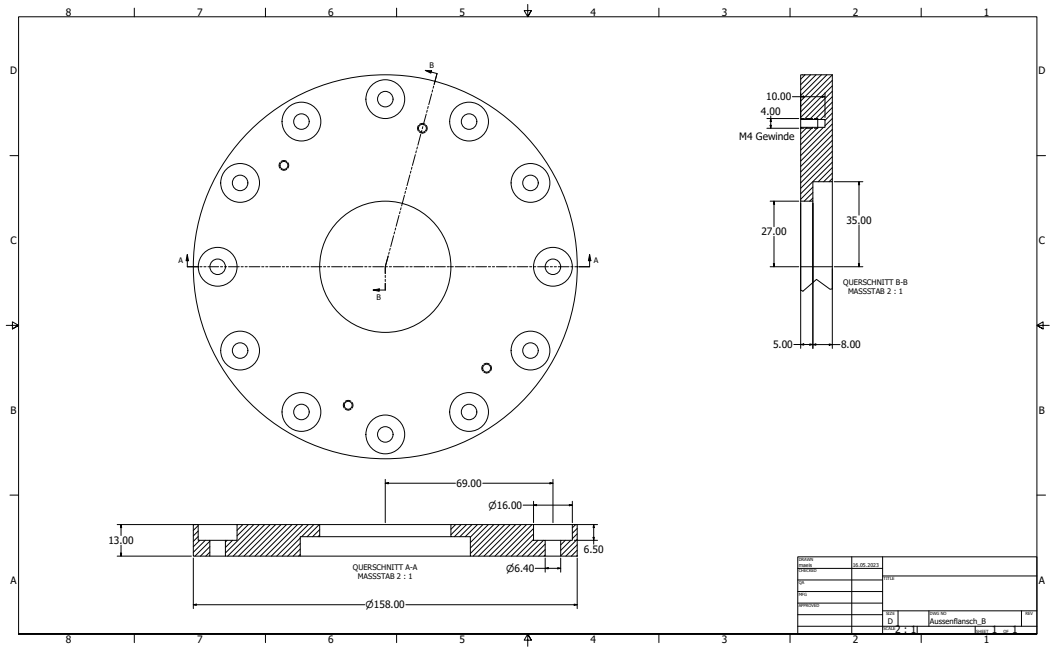

(b)

Fig. A.2.: Outer flange

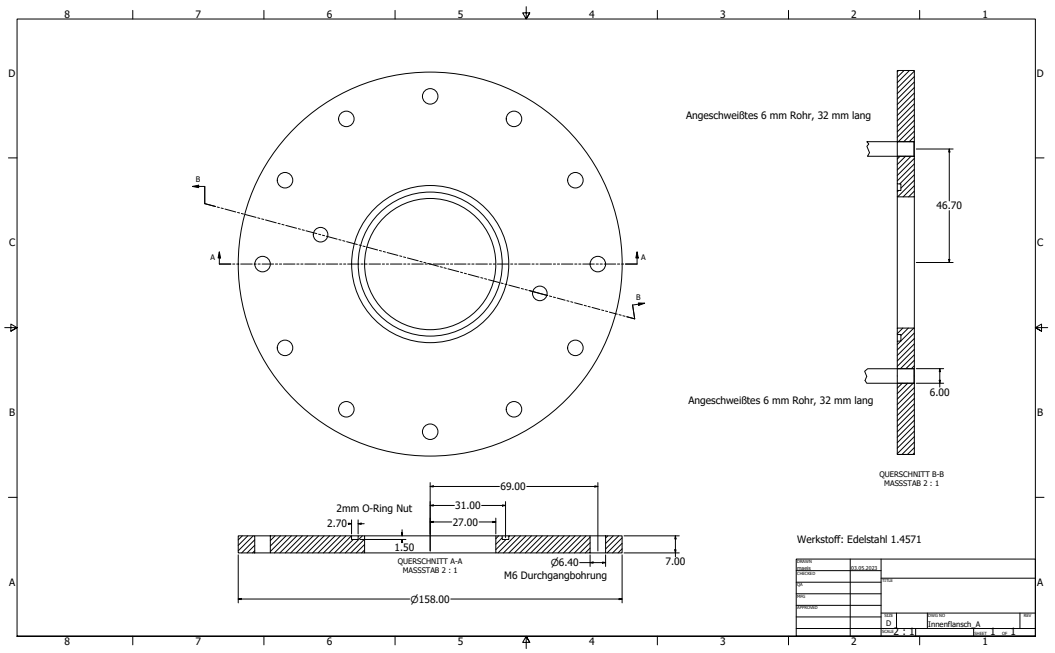

(a)

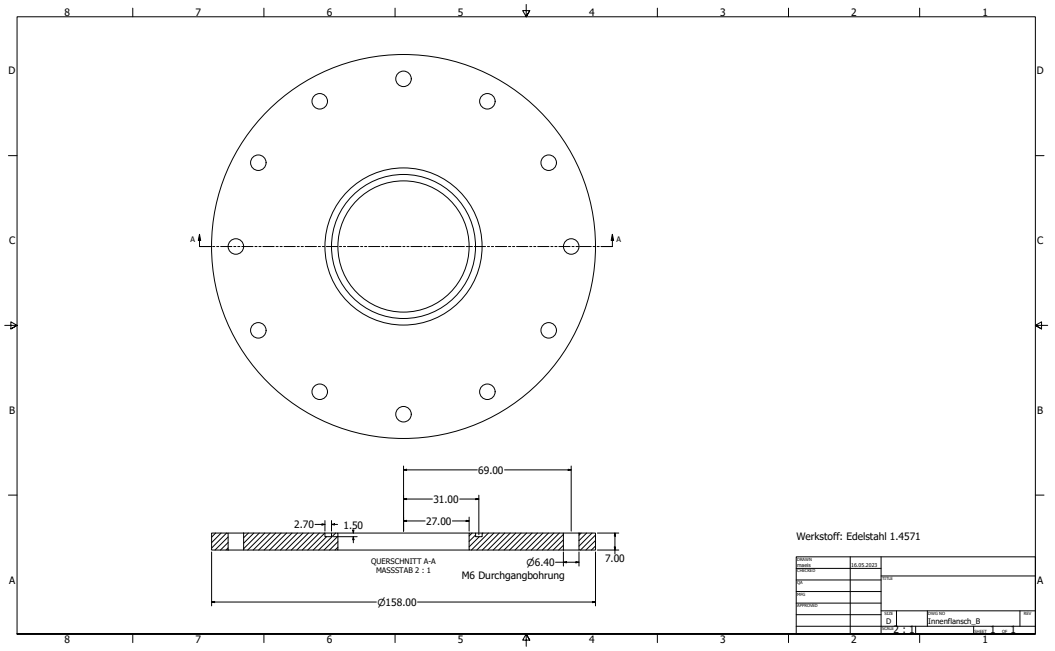

(b) Inner flange

Fig. A.3.

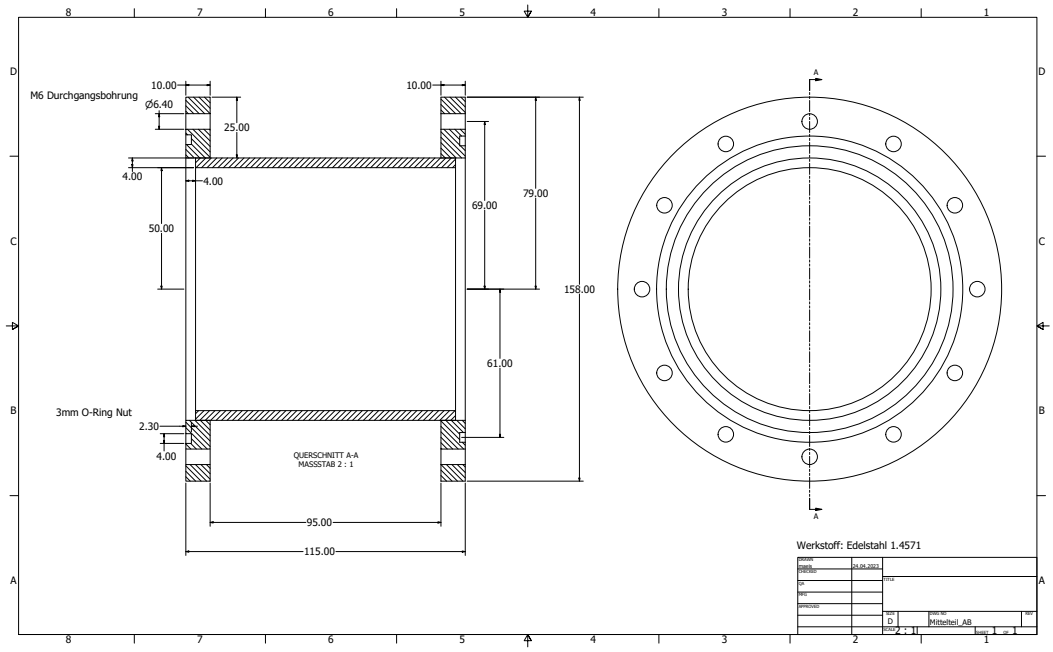

Fig. A.4.: Main Body of the test cell

Colophon

This thesis was typeset with LaTeX 2_ε. It uses the *Clean Thesis* style developed by Ricardo Langner. The design of the *Clean Thesis* style is inspired by user guide documents from Apple Inc.

Download the *Clean Thesis* style at `http://cleanthesis.der-ric.de/`.

Declaration

Ich versichere, dass ich die Arbeit selbstständig verfasst und keine anderen als die angegebenen Quellen und Hilfsmittel benutzt sowie Zitate kenntlich gemacht habe.

Mainz, Mai 13, 2024

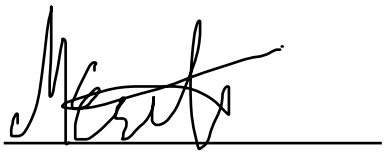

Magdalena Eisenhuth